

# Hierarchical Representations with Poincaré Variational Auto-Encoders

Emile Mathieu<sup>†</sup>

emile.mathieu@stats.ox.ac.uk

Charline Le Lan<sup>†</sup>

charline.lelan@stats.ox.ac.uk

Chris J. Maddison<sup>†\*</sup>

cmaddis@stats.ox.ac.uk

Ryota Tomioka<sup>‡</sup>

ryoto@microsoft.com

Yee Whye Teh<sup>†\*</sup>

y.w.teh@stats.ox.ac.uk

<sup>†</sup> Department of Statistics, University of Oxford, United Kingdom

\* DeepMind, London, United Kingdom

<sup>‡</sup> Microsoft Research, Cambridge, United Kingdom

## Abstract

The variational auto-encoder (VAE) model is a popular method to learn at once a generative model and embeddings for data living in a high-dimensional space. In the real world, many datasets may be assumed to be hierarchically structured. Traditionally, VAEs use a Euclidean latent space, but tree-like structures cannot be efficiently embedded in such spaces as opposed to hyperbolic spaces with negative curvature. We therefore endow VAEs with a Poincaré ball model of hyperbolic geometry and derive the necessary methods to work with two main Gaussian generalisations on that space. We empirically show better generalisation to unseen data than the Euclidean counterpart, and can qualitatively and quantitatively better recover hierarchical structures.

## 1 INTRODUCTION

Learning useful representation from unlabelled raw sensory observations, which are often high-dimensional, is a problem of significant importance in machine learning. Variational auto-encoders (VAEs) (Kingma and Welling, 2013; Rezende et al., 2014) are a popular approach to this; they are probabilistic generative models composed of an *encoder* stochastically embedding observations in a low dimensional latent space  $\mathcal{Z}$ , and a *decoder* generating observations  $\mathbf{x} \in \mathcal{X}$  from encodings  $\mathbf{z} \in \mathcal{Z}$ . After training, the encodings constitute a low-dimensional representation

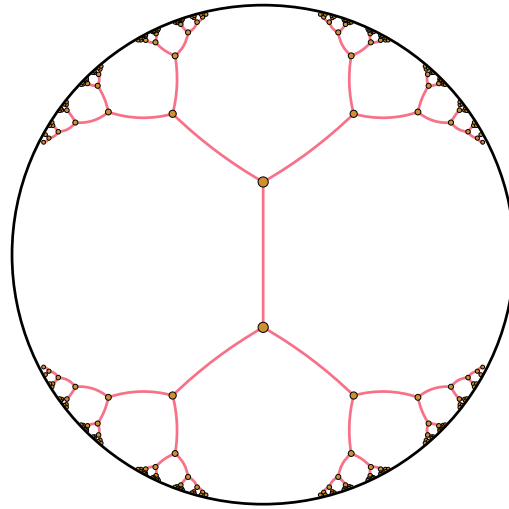


Figure 1: A regular tree isometrically embedded in the Poincaré disc. Red curves are same length *geodesics*, i.e. "straight lines".

of the original raw observations, which can be used as features for a downstream task (e.g. Huang and LeCun, 2006; Coates et al., 2011) or be interpretable for their own sake. VAEs are therefore of interest for representation learning (Bengio et al., 2013), a field which aims to learn *good representations*, e.g. interpretable representations, ones yielding better generalisation, or ones useful as a pre-processing task.

It can be argued that in many domains data should be represented hierarchically. For example, in cognitive science it is widely accepted that human beings organise object

categories hierarchically (e.g. Roy et al., 2006; Collins and Quillian, 1969; Keil, 1979). In biology, the theory of evolution (Darwin, 1859) implies that features of living organisms are related in a hierarchical manner given by the evolutionary tree. Unsurprisingly, explicitly incorporating hierarchical structure in probabilistic models has been a long-running research topic (e.g. Duda et al., 2000; Heller and Ghahramani, 2005).

This earlier work has tended to use trees as data structures to represent hierarchies. Recently, hyperbolic spaces have been proposed as an alternative approach to learn hierarchical representations from textual and graph-structured data (Nickel and Kiela, 2017). Hyperbolic spaces can be thought of as continuous versions of trees or vice versa, as illustrated in Figure 1. Hence, trees can be embedded with arbitrarily low error into the Poincaré disc model of hyperbolic geometry (Sarkar, 2012). The exponential growth of the Poincaré surface area with respect to its radius is also related with the exponential growth of leaves in a tree with respect to its depth. Further, these spaces are smooth, enabling the use of deep learning approaches which rely on differentiability.

Hence we suggest that a VAE endowed with a hyperbolic latent space will be more capable at representing and discovering hierarchies. This is what we consider in this work. Our goals are twofold; (a) learn a latent representation that is interpretable in terms of hierarchical relationships among the observations, (b) yield a more "compact" (than its Euclidean counterpart) representation for low dimensional latent spaces – therefore yielding better reconstructions – for data having such an underlying hierarchical structure. Our main contributions are as follow:

1. We propose efficient and reparametrisable sampling schemes, as well as calculate the probability density functions, for two main isotropic Gaussian generalisations defined on the Poincaré ball, namely the maximum-entropy and wrapped normal distributions. These are the required ingredients for learning our VAEs.
2. We empirically demonstrate that endowing a VAE with a Poincaré ball latent space can be beneficial in terms of model generalisation and can yield more interpretable representations.

Our work fits well with a surge in interest of combining hyperbolic geometry and VAEs. Of these, it related most strongly to the concurrent and very recent works of Ovinnikov (2018); Grattarola et al. (2018); Nagano et al. (2019). Our approach varies from the first two articles by considering a VAE framework where we maximise a

lower bound on the marginal likelihood, as opposed to respectively a Wasserstein and an adversarial auto-encoder setting. It also differs from Nagano et al. (2019) by considering the *maximum entropy normal* generalisation along with the *wrapped normal*, and by designing a decoder which takes into account the latent space geometry. We discuss these works in more detail in Section 4.

The remainder of this paper is organized as follows: In Section 2, we briefly review Riemannian geometry and the Poincaré ball model of hyperbolic geometry. In Section 3, we introduce our Poincaré VAE model, and discuss its design and how it can be trained. Sections 4 discusses related works, and Section 5 empirically assesses the performance of our model on a synthetic dataset generated from a branching diffusion process, as well as on MNIST. Finally, Section 6 concludes with a discussion and future works.

## 2 THE POINCARÉ BALL MODEL OF HYPERBOLIC GEOMETRY

### 2.1 REVIEW OF RIEMANNIAN GEOMETRY

A real, smooth *manifold*  $\mathcal{M}$  is a collection of real vectors  $\mathbf{x}$ , which is locally similar to a linear space. At each point  $\mathbf{x}$  of the manifold  $\mathcal{M}$  is defined a real vector space of the same dimensionality as  $\mathcal{M}$ , called the *tangent space* in  $\mathbf{x}$ :  $\mathcal{T}_{\mathbf{x}}\mathcal{M}$ . Intuitively, it contains all the possible directions in which one can tangentially pass through  $\mathbf{x}$ . For each point  $\mathbf{x}$  of the manifold, the *metric tensor*  $\mathbf{g}(\mathbf{x})$  defines an inner product on the associated tangent space:  $\langle \cdot, \cdot \rangle_{\mathbf{x}} : \mathcal{T}_{\mathbf{x}}\mathcal{M} \times \mathcal{T}_{\mathbf{x}}\mathcal{M} \rightarrow \mathcal{M}$ . A *Riemannian manifold* is then defined as a tuple  $(\mathcal{M}, \mathbf{g})$  (Petersen, 2006).

The metric tensor gives *local* notions of angle, length of curves, surface area and volume, from which *global* quantities can be derived by integrating local contributions. A norm is induced by the inner product on  $\mathcal{T}_{\mathbf{x}}\mathcal{M}$ :  $\|\cdot\|_{\mathbf{x}} = \sqrt{\langle \cdot, \cdot \rangle_{\mathbf{x}}}$ . The *matrix representation of the Riemannian metric*  $G(\mathbf{x})$ , is defined such that  $\forall \mathbf{u}, \mathbf{v} \in \mathcal{T}_{\mathbf{x}}\mathcal{M} \times \mathcal{T}_{\mathbf{x}}\mathcal{M}$ ,  $\mathbf{g}(\mathbf{x})(\mathbf{u}, \mathbf{v}) = \langle \mathbf{u}, \mathbf{v} \rangle_{\mathbf{x}} = \mathbf{u}^T G(\mathbf{x}) \mathbf{v}$ . An infinitesimal volume element is induced on each tangent space  $\mathcal{T}_{\mathbf{x}}\mathcal{M}$ , and thus a measure  $d\mathcal{M}(\mathbf{x}) = \sqrt{|G(\mathbf{x})|} d\mathbf{x}$  on the manifold, with  $d\mathbf{x}$  being the Lebesgue measure.

The length of a curve  $\gamma : t \mapsto \gamma(t) \in \mathcal{M}$  is given by

$$L(\gamma) = \int_0^1 \|\gamma'(t)\|_{\gamma(t)}^{1/2} dt.$$

The concept of straight lines can then be generalised to *geodesics*, which are constant speed curves giving the shortest path between pairs of points  $\mathbf{x}, \mathbf{y}$  of the manifold:  $\gamma^* = \arg \min L(\gamma)$  with  $\gamma(0) = \mathbf{x}$ ,  $\gamma(1) = \mathbf{y}$

and  $\|\gamma'(t)\|_{\gamma(t)} = 1$ . A *global* distance is thus induced on  $\mathcal{M}$  given by  $d_{\mathcal{M}}(\mathbf{x}, \mathbf{y}) = \inf L(\gamma)$ . Endowing  $\mathcal{M}$  with that distance consequently defines a metric space  $(\mathcal{M}, d_{\mathcal{M}})$ . The concept of moving along a "straight" curve with constant velocity is given by the *exponential map*. In particular, there is a unique unit speed *geodesic*  $\gamma$  satisfying  $\gamma(0) = \mathbf{x}$  with initial tangent vector  $\gamma'(0) = \mathbf{v}$ . The corresponding exponential map is then defined by  $\exp_{\mathbf{x}}(\mathbf{v}) = \gamma(1)$ , as illustrated on Figure 2. The *logarithm map* is the inverse  $\log_{\mathbf{x}} = \exp_{\mathbf{x}}^{-1} : \mathcal{M} \rightarrow \mathcal{T}_{\mathbf{x}}\mathcal{M}$ . For geodesically complete manifolds, such as the Poincaré ball,  $\exp_{\mathbf{x}}$  is well-defined on the full tangent space  $\mathcal{T}_{\mathbf{x}}\mathcal{M}$ .

## 2.2 THE HYPERBOLIC SPACE

From a historical perspective, hyperbolic geometry was created in the first half of the nineteenth century in the midst of attempts to understand Euclid's axiomatic basis for geometry (Coxeter, 1942). It is one type of non-Euclidean geometry, the one that discards Euclid's *fifth postulate* (or *parallel postulate*) to replace it with the following one: *Given a line and a point not on it, there is more than one line going through the given point that is parallel to the given line.*

In contrast with the hypersphere  $\mathbb{S}^d$  and the Euclidean space  $\mathbb{R}^d$ , the hyperbolic space  $\mathbb{H}^d$  can be constructed using various isomorphic models (none of which is prevalent), among them the hyperboloid model, the Beltrami-Klein model, the Poincaré half-plane model and the Poincaré ball (Beltrami, 1868) which we will be relying on.

Intuitively, hyperbolic spaces can be thought of as continuous versions of trees or vice versa, trees can be thought of as "discrete hyperbolic spaces", as illustrated in Figure 1. Indeed, trees can be embedded with arbitrarily low distortion<sup>1</sup> into the Poincaré disc (Sarkar, 2012). In contrast, Bourgain's theorem (Linial et al., 1994) shows that the Euclidean space is unable to obtain comparably low distortion for trees - even using an unbounded number of dimensions. This type of structure is naturally suited with hyperbolic spaces since the volume and surface area grow exponentially with their radius.

## 2.3 THE POINCARÉ BALL

The d-dimensional Poincaré ball  $\mathcal{B}_c^d$  is a model of the hyperbolic space  $\mathbb{H}^d$  with curvature  $c$ . Throughout the paper we will denote the Euclidean norm and inner product

<sup>1</sup>Global metric for graph embeddings, measuring relative difference between pairwise distances in the embedding space and in the original space, the best distortion being 0.

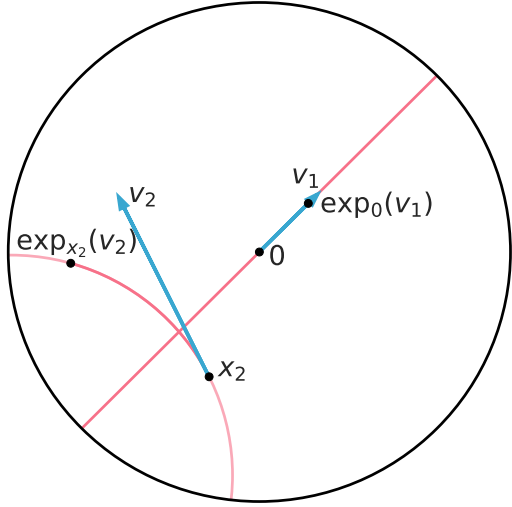


Figure 2: Some geodesics and exponential maps in the Poincaré disc.

respectively by  $\|\cdot\|$  and  $\langle \cdot, \cdot \rangle$ . The Poincaré ball *metric tensor* is a conformal<sup>2</sup> one, given by

$$\mathfrak{g}_p^c(\mathbf{x}) = \left( \frac{2}{1 - c \|\mathbf{x}\|^2} \right)^2 \mathfrak{g}_e = (\lambda_{\mathbf{x}}^c)^2 \mathfrak{g}_e, \quad (1)$$

where  $\lambda_{\mathbf{x}}^c = \frac{2}{1 - c \|\mathbf{x}\|^2}$ ,  $\mathbf{x} \in \mathcal{B}_c^d$  and  $\mathfrak{g}_e$  denotes the Euclidean metric tensor, i.e. the usual dot product,  $\forall \mathbf{u}, \mathbf{v} \in \mathbb{R}^d \mathfrak{g}_e(\mathbf{u}, \mathbf{v}) = \langle \mathbf{u}, \mathbf{v} \rangle$ . The Poincaré ball model of hyperbolic space corresponds then to the Riemannian manifold  $\mathbb{B}_c^d = (\mathcal{B}_c^d, \mathfrak{g}_p^c)$ . The induced *distance* function between  $\mathbf{x}, \mathbf{y} \in \mathcal{B}_c^d$  is given as

$$d_p^c(\mathbf{x}, \mathbf{y}) = \frac{1}{\sqrt{c}} \cosh^{-1} \left( 1 + \frac{2c\|\mathbf{x} - \mathbf{y}\|^2}{(1 - c\|\mathbf{x}\|^2)(1 - c\|\mathbf{y}\|^2)} \right).$$

The framework of *gyrovector spaces* provides a non-associative algebraic formalism for hyperbolic geometry, analogous to the vector space structure of Euclidean geometry (Ungar, 2008). The *Möbius addition* of  $\mathbf{x}$  and  $\mathbf{y}$  in  $\mathbb{B}_c^d$  is defined as

$$\mathbf{x} \oplus_c \mathbf{y} = \frac{(1 + 2c\langle \mathbf{x}, \mathbf{y} \rangle + c\|\mathbf{y}\|^2)\mathbf{x} + (1 - c\|\mathbf{x}\|^2)\mathbf{y}}{1 + 2c\langle \mathbf{x}, \mathbf{y} \rangle + c^2\|\mathbf{x}\|^2\|\mathbf{y}\|^2}.$$

One recovers the Euclidean addition of two vectors in  $\mathbb{R}^d$  as  $c \rightarrow 0$ . Building on that framework, Ganea et al. (2018) derived closed-form formulations for the *exponential map*

<sup>2</sup>i.e. proportional to the Euclidean metric tensor  $\mathfrak{g}_e$ .

(illustrated in Figure 2)

$$\begin{aligned}\exp_{\mathbf{x}}^c(\mathbf{v}) &= \mathbf{x} \oplus_c \left( \tanh \left( \sqrt{c} \frac{\lambda_{\mathbf{x}}^c \|\mathbf{v}\|}{2} \right) \frac{\mathbf{v}}{\sqrt{c} \|\mathbf{v}\|} \right), \\ \exp_{\mathbf{0}}^c(\mathbf{v}) &= \tanh \left( \sqrt{c} \|\mathbf{v}\| \right) \frac{\mathbf{v}}{\sqrt{c} \|\mathbf{v}\|}\end{aligned}$$

and its inverse, the *logarithm map*

$$\begin{aligned}\log_{\mathbf{x}}^c(\mathbf{y}) &= \frac{2}{\sqrt{c} \lambda_{\mathbf{x}}^c} \tanh^{-1} \left( \sqrt{c} \|\mathbf{x} \oplus_c \mathbf{y}\| \right) \frac{-\mathbf{x} \oplus_c \mathbf{y}}{\|\mathbf{x} \oplus_c \mathbf{y}\|}, \\ \log_{\mathbf{0}}^c(\mathbf{y}) &= \tanh^{-1} \left( \sqrt{c} \|\mathbf{y}\| \right) \frac{\mathbf{y}}{\sqrt{c} \|\mathbf{y}\|}.\end{aligned}$$

### 3 THE POINCARÉ VAE

We consider the problem of mapping an empirical observations distribution to a lower dimensional Poincaré ball  $\mathbb{B}_c^d$ , as well as learning a map from this latent space  $\mathcal{Z} = \mathbb{B}_c^d$  to the observation space  $\mathcal{X}$ . Building on the VAE framework, this *Poincaré-VAE* model, or  $\mathcal{P}^c$ -VAE for short, only differs by the choice of prior distribution  $p(\cdot)$  and posterior distribution  $q_{\phi}(\cdot | \mathbf{x})$  which are defined on  $\mathbb{B}_c^d$ , and by the encoder  $g_{\phi}$  and decoder  $f_{\theta}$  maps which take into account the geometry of the latent space. Their parameters  $\{\theta, \phi\}$  are learned by maximising the *evidence lower bound* (ELBO). Hyperbolic geometry is in a sense an extrapolation of Euclidean geometry. Hence our model can also be seen as a generalisation of a usual Euclidean VAE that we denote by  $\mathcal{N}$ -VAE, i.e.  $\mathcal{P}^c$ -VAE  $\xrightarrow[c \rightarrow 0]{} \mathcal{N}$ -VAE.

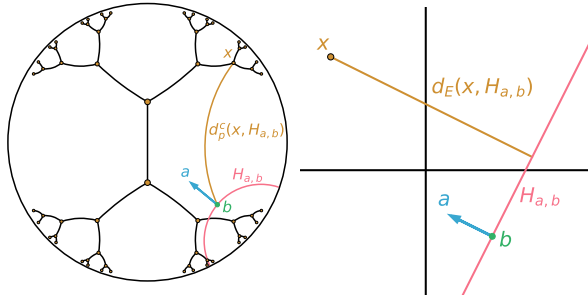


Figure 3: Illustration of an orthogonal projection on a hyperplane in a Poincaré disc  $\mathbb{B}_c^2$  (Left) and an Euclidean plane (Right). Those hyperplanes are *decision boundaries*.

#### 3.1 PRIOR AND VARIATIONAL POSTERIOR DISTRIBUTIONS

In order to parametrise distributions on the Poincaré ball, we consider two main generalisations of normal distribu-

tions. A more detailed review of Gaussian generalisations on manifold can be found in Appendix B.1.

**Riemannian normal** One generalisation is the distribution maximising entropy with a given expectation and variance (Said et al., 2014; Pennec, 2006; Hauberg, 2018), often called *Riemannian normal* distribution, with density w.r.t the metric induced measure  $d\mathcal{M}$ , given by

$$\begin{aligned}\frac{d\nu^R(\mathbf{x}|\boldsymbol{\mu}, \sigma^2)}{d\mathcal{M}(\mathbf{x})} &= \mathcal{N}_{\mathbb{B}_c^d}^R(\mathbf{x}|\boldsymbol{\mu}, \sigma^2) \\ &= \frac{1}{Z^R} \exp \left( -\frac{d_p^c(\boldsymbol{\mu}, \mathbf{x})^2}{2\sigma^2} \right),\end{aligned}\quad (2)$$

with  $\sigma > 0$  a dispersion parameter,  $\boldsymbol{\mu} \in \mathbb{B}_c^d$  the Fréchet expectation<sup>3</sup>, and  $Z^R$  the normalising constant derived in Appendix B.7, given by

$$\begin{aligned}Z^R &= \frac{2\pi^{d/2}}{\Gamma(d/2)} \times \sqrt{\frac{\pi}{2}} \sigma \frac{1}{(2\sqrt{c})^{d-1}} \sum_{k=0}^{d-1} (-1)^k \binom{d-1}{k} \\ &\quad e^{\frac{(d-1-2k)^2}{2} c \sigma^2} \left[ 1 + \text{erf} \left( \frac{(d-1-2k)\sqrt{c}\sigma}{\sqrt{2}} \right) \right].\end{aligned}$$

Figure 4 shows samples from such a *Riemannian normal* distribution.

**Wrapped normal** Another generalisation is to consider a normal distribution on the tangent space  $\mathcal{T}_{\boldsymbol{\mu}}\mathcal{M}$  at the expectation  $\boldsymbol{\mu}$  and then to pushforward this measure via the *exponential map* back on the manifold. That distribution is often referred as a *wrapped normal* distribution, and has been used in auto-encoder frameworks with other manifolds (Grattarola et al., 2018; Nagano et al., 2019; Falorsi et al., 2018). Samples  $\mathbf{x} \in \mathbb{B}_c^d$  are by definition obtained as

$$\begin{aligned}\mathbf{x} &= \exp_{\boldsymbol{\mu}}^c \left( \frac{\mathbf{v}}{\lambda_{\boldsymbol{\mu}}^c} \right) = \left( \frac{r}{\lambda_{\boldsymbol{\mu}}^c} \boldsymbol{\alpha} \right) \\ \text{with } \mathbf{v} &\sim \mathcal{N}(\mathbf{0}, \sigma^2), r = \|\mathbf{v}\| \text{ and } \boldsymbol{\alpha} = \mathbf{v}/\|\mathbf{v}\|.\end{aligned}$$

Its pdf is given by (details given in Appendix B.3)

$$\begin{aligned}\frac{d\nu^W(\mathbf{x}|\boldsymbol{\mu}, \sigma^2)}{d\mathcal{M}(\mathbf{x})} &= \mathcal{N}_{\mathbb{B}_c^d}^W(\mathbf{x}|\boldsymbol{\mu}, \sigma^2) \\ &= \frac{1}{(\sqrt{2\pi}\sigma)^d} e^{-d_p^c(\boldsymbol{\mu}, \mathbf{x})^2/2\sigma^2} \left( \frac{\sqrt{c} d_p^c(\boldsymbol{\mu}, \mathbf{x})}{\sinh(\sqrt{c} d_p^c(\boldsymbol{\mu}, \mathbf{x}))} \right)^{d-1}.\end{aligned}\quad (3)$$

The standard normal distribution is recovered for both generalisations as  $c \rightarrow 0$ . We discuss the pros and

<sup>3</sup>Generalisation of the expectation to manifolds, defined as minimisers of  $\sigma^2(\boldsymbol{\mu}) = \int_{\mathcal{M}} d_{\mathcal{M}}(\boldsymbol{\mu}, \mathbf{x})^2 p(\mathbf{x}) d\mathcal{M}(\mathbf{x})$ .

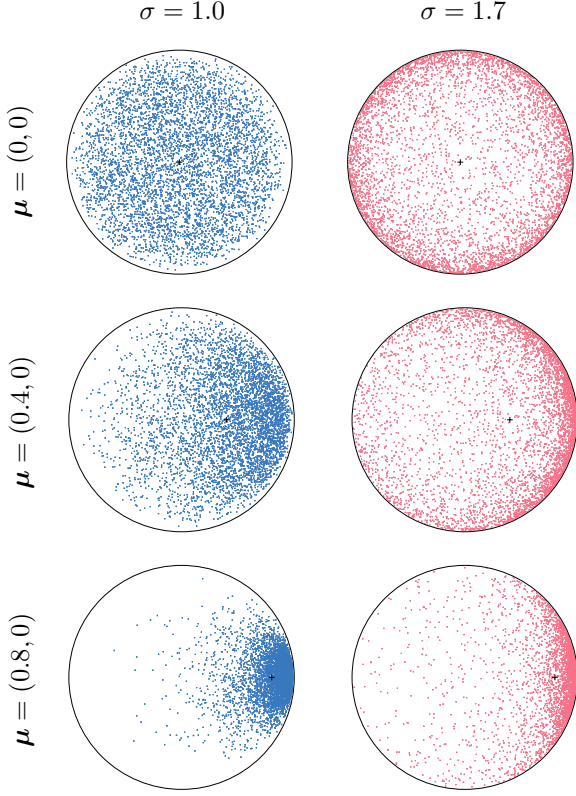


Figure 4: Samples from *Riemannian normal* distributions with different expectations  $\mu$  (black crosses) and distortions  $\sigma$ .

cons of those two distributions in Appendix B.1. We refer to both as *hyperbolic normal* distributions with pdf  $\mathcal{N}_{\mathbb{B}_c^d}(\mathbf{x}|\mu, \sigma^2)$ .

Hence, the prior distribution is chosen to be a hyperbolic normal distribution with mean zero,  $p(\mathbf{z}) = \mathcal{N}_{\mathbb{B}_c^d}(\cdot|\mathbf{0}, \sigma_0^2)$ , and the variational family to be  $\mathcal{Q} = \{\mathcal{N}_{\mathbb{B}_c^d}(\cdot|\mu, \sigma^2) \mid \mu \in \mathbb{B}_c^d, \sigma > 0\}$ .

### 3.2 ENCODER AND DECODER ARCHITECTURE

We make use of two neural networks, a *decoder*  $f_\theta$  and an *encoder*  $g_\phi$ , to respectively parametrise the likelihood  $p(\cdot|f_\theta(\mathbf{z})) : \mathcal{Z} \rightarrow \mathcal{P}(\mathcal{X})$  and the variational posterior  $q(\cdot|g_\phi(\mathbf{x})) : \mathcal{X} \rightarrow \mathcal{P}(\mathcal{Z}) \in \mathcal{Q}$ . The input of  $f_\theta$  and the output of  $g_\phi$  need to respect the hyperbolic geometry of  $\mathcal{Z}$ . In the following we describe appropriate choices for the first layer of the decoder and the last layer of the encoder respecting the geometry.

**Decoder** In the Euclidean case, an affine transformation can be written in the form  $f_{\mathbf{a}, \mathbf{b}}(\mathbf{x}) = \langle \mathbf{a}, \mathbf{x} - \mathbf{b} \rangle$ , with orientation and offset parameters  $\mathbf{a}, \mathbf{b} \in \mathbb{R}^d$ . This can be rewritten in the form

$$f_{\mathbf{a}, \mathbf{b}}(\mathbf{x}) = \text{sign}(\langle \mathbf{a}, \mathbf{x} - \mathbf{b} \rangle) \|\mathbf{a}\| d_E(\mathbf{x}, H_{\mathbf{a}, \mathbf{b}}^c)$$

where  $H_{\mathbf{a}, \mathbf{b}}^c = \{\mathbf{x} \in \mathbb{R}^p \mid \langle \mathbf{a}, \mathbf{x} - \mathbf{b} \rangle = 0\} = \mathbf{b} + \{\mathbf{a}\}^\perp$  is the decision hyperplane. The third term refers to the distance between  $\mathbf{x}$  and the decision hyperplane  $H_{\mathbf{a}, \mathbf{b}}^c$ , and the first to the side of  $H_{\mathbf{a}, \mathbf{b}}^c$  where  $\mathbf{x}$  lies. Ganea et al. (2018) analogously introduced an operator  $f_{\mathbf{a}, \mathbf{b}}^c : \mathbb{B}_c^d \rightarrow \mathbb{R}^p$  on the Poincaré ball,

$$f_{\mathbf{a}, \mathbf{b}}^c(\mathbf{x}) = \text{sign}(\langle \mathbf{a}, \log_{\mathbf{x}}^c(\mathbf{b}) \rangle) \|\mathbf{a}\|_b d_p^c(\mathbf{x}, H_{\mathbf{a}, \mathbf{b}}^c)$$

$$H_{\mathbf{a}, \mathbf{b}}^c = \{\mathbf{x} \in \mathbb{B}_c^d \mid \langle \mathbf{a}, \log_{\mathbf{x}}^c(\mathbf{b}) \rangle = 0\} = \exp_{\mathbf{b}}^c(\{\mathbf{a}\}^\perp).$$

A closed-formed expression for the distance  $d_p^c(\mathbf{x}, H_{\mathbf{a}, \mathbf{b}}^c)$  was also derived,

$$d_p^c(\mathbf{x}, H_{\mathbf{a}, \mathbf{b}}^c) = \frac{1}{\sqrt{c}} \sinh^{-1} \left( \frac{2\sqrt{c} |\langle -\mathbf{b} \oplus_c \mathbf{x}, \mathbf{a} \rangle|}{(1 - c \|\mathbf{b} \oplus_c \mathbf{x}\|^2) \|\mathbf{a}\|} \right).$$

The decision boundary  $H_{\mathbf{a}, \mathbf{b}}^c$  is called a called *gyroplanes* and is a semi-hypersphere orthogonal to the Poincaré ball's boundary as illustrated on Figure 3. The decoder's first layer is a concatenation of such operators, which are then fed to a standard neural network.

**Encoder** The encoder  $g_\phi$  outputs a Fréchet expectation  $\mu \in \mathbb{B}_c^d$  and a distortion  $\sigma \in \mathbb{R}_+^*$  which parametrise the hyperbolic variational posterior. We classically constrain  $\sigma$  via a *Softplus* parametrisation. The Fréchet expectation is obtained as the image of the exponential map  $\exp_{\mathbf{0}}$ .

### 3.3 TRAINING

We follow a standard variational approach by deriving a lower bound on the marginal likelihood, which is then optimised using the reparametrisation trick. The two non trivial parts in our setting is to reparametrise the variational family and to compute log densities.

**Objective** The *evidence lower bound* (ELBO) can readily be extended for Riemannian latent spaces by applying Jensen's inequality w.r.t.  $d\mathcal{M}$  (see Appendix A) yielding

$$\log p(\mathbf{x}) \geq \mathcal{L}_{\mathcal{M}}(\mathbf{x}; \theta, \phi) \quad (4)$$

$$\triangleq \int_{\mathcal{M}} \ln \left( \frac{p_\theta(\mathbf{x}|\mathbf{z})p(\mathbf{z})}{q_\phi(\mathbf{z}|\mathbf{x})} \right) q_\phi(\mathbf{z}|\mathbf{x}) d\mathcal{M}(\mathbf{z}).$$

The densities have been derived earlier in Equations 11 and 14. Hence we can compute an unbiased estimate of

$\mathcal{L}_{\mathcal{M}}(\mathbf{x}; \theta, \phi)$  with Monte carlo (MC) samples. In the following paragraphs, we describe a reparametrisable sampling scheme for both hyperbolic normal distributions.

---

**Algorithm 1** Hyperbolic normal sampling scheme

---

**Require:**  $\mu, \sigma^2$ , dimension  $d$ , curvature  $c$

- 1: **if** Wrapped normal **then**
- 2:    $\mathbf{v} \sim \mathcal{N}(\mathbf{0}_d, \sigma^2)$
- 3: **else if** Riemannian normal **then**
- 4:   Let's  $g$  be a piecewise exponential proposal
- 5:   **while** sample  $r$  not accepted **do**
- 6:     Propose  $r \sim g(\cdot)$ ,  $u \sim \mathcal{U}([0, 1])$
- 7:     **if**  $u < \frac{\rho^R(r)}{g(r)}$  **then** Accept sample  $r$
- 8:     **else** Reject sample  $r$
- 9:     **end if**
- 10: **end while**
- 11: Sample direction  $\alpha \sim \mathcal{U}(\mathbb{S}^{d-1})$
- 12:    $\mathbf{v} \leftarrow r\alpha$
- 13: **end if**
- 14:  $\mathbf{z} \leftarrow \exp_{\mu}^c \left( \frac{\mathbf{v}}{\lambda_{\mu}^c} \right)$
- 15: Return  $\mathbf{z}$

---

**Sampling** In the Euclidean setting, by working in polar coordinates, an isotropic normal distribution centred at  $\mu$  can be described by a directional vector  $\alpha$  uniformly distributed on the hypersphere and a univariate radius  $r = d_E(\mu, \mathbf{x})$  following a Chi-squared distribution. In the Poincaré ball we can rely on a similar representation, through a *hyperbolic polar* change of coordinates given by

$$\mathbf{x} = \exp_{\mu}^c \left( \frac{r}{\lambda_{\mu}^c} \alpha \right). \quad (5)$$

The direction  $\alpha$  is still uniformly distributed on the hypersphere and for the *wrapped normal*, the radius  $r = d_p^c(\mu, \mathbf{x})$  is by definition still Chi-squared distributed,

$$\rho^W(r) \propto \mathbb{1}_{\mathbb{R}_+}(r) e^{-\frac{r^2}{2\sigma^2}} r^{d-1}, \quad (6)$$

while for the *Riemannian normal* its density is given by (derivations given in Appendix B.4)

$$\rho^R(r) \propto \mathbb{1}_{\mathbb{R}_+}(r) e^{-\frac{r^2}{2\sigma^2}} \left( \frac{\sinh(\sqrt{c}r)}{\sqrt{c}} \right)^{d-1}. \quad (7)$$

This density can efficiently be sampled with a piecewise exponential distribution proposal which makes use of the log-concavity. The *Riemannian normal* sampling scheme is not directly affected by dimensionality since the radius is a uni-dimensional variable. Full sampling schemes are described in Algorithm 1 and Appendix B.8.

**Reparametrisation** Using the exponential map reparametrisation (Eq 5), gradients  $\nabla_{\mu} \mathbf{x}$  can straightforwardly be computed. Gradients with respect to the dispersion  $\nabla_{\sigma} \mathbf{x}$  are readily available for the *wrapped normal* using the reparametrisation of the Gaussian distribution. For the *Riemannian normal*, we additionally rely on an implicit reparametrisation (Figurnov et al., 2018) of  $\rho^R$  via its cdf  $F^R(r|\sigma)$ .

## 4 RELATED WORK

In the Bayesian Nonparametric's literature, explicitly modelling the hierarchical structure of data has been a long-going trend (Teh et al., 2008; Heller and Ghahramani, 2005; Griffiths et al., 2004; Ghahramani et al., 2010; Larsen et al., 2001; Salakhutdinov et al., 2011). The discreteness of trees used in such models makes learning difficult, whereas performing optimisation in a continuous hyperbolic space is an attractive alternative.

Embedding graphs in hyperbolic spaces has been empirically shown (Nickel and Kiela, 2017, 2018; Chamberlain et al., 2017) to yield a more efficient representation compared to Euclidean spaces, especially for low dimensions. Similarly, word embeddings have been shown to potentially gain from hyperbolic geometry (Tifrea et al., 2018). De Sa et al. (2018) studied the trade-offs of tree embeddings in the Poincaré disc.

VAEs with non Euclidean latent space have first been explored by Davidson et al. (2018), endowing the latent space with a hyperspherical geometry, and parametrising variational posteriors with Von-Mises Fisher distributions. Still, in the VAE setting, Lie groups as latent space have been proposed by Falorsi et al. (2018), where embedding rotational structure through the  $SO(3)$  group is given a particular focus.

Independent works recently considered endowing auto-encoders (AEs) latent space with a hyperbolic geometry in order to yield a hierarchical representation. Grattarola et al. (2018) considered constant curvature manifolds (CCMs) (i.e. hyperspherical, Euclidean and hyperboloid models) as latent space within an adversarial auto-encoder. So as to be able to rely on generic neural networks, the encoder is regularised to make its outputs close to the manifold. On the counterpart, the encoder and decoder architectures are thus not tailored to take into account the geometry of the latent space. Embeddings are regularised towards the prior distribution via a *discriminator*, which requires the design and training of an extra neural network.

Ovinnikov (2018) recently proposed to similarly endow

VAEs latent space with a Poincaré ball model. The model is trained by minimising a Wasserstein Auto-Encoder loss (Tolstikhin et al., 2017) with a MMD regularisation because a close-form solution of the ELBO’s entropy term cannot be derived. We instead rely on a MC approximation of the ELBO. A *Möbius* neural-network architecture, proposed by Ganea et al. (2018), is used to parametrise the decoder.

Recently, Nagano et al. (2019) proposed to use a *wrapped* normal distribution to model uncertainty on the *hyperboloid* model of hyperbolic space. They derive its pdf and a reparametrisable sampling scheme, allowing such a distribution to be used in a variational learning framework. They apply this *wrapped* normal distribution to stochastically embed graphs and to parametrise the variational family in VAEs.

Distributions defined on manifolds are of interest to model uncertainty of data living on such spaces (either intrinsically or assumed to), e.g. directional statistics (Ley and Verdebout, 2017; Mardia and Jupp, 2009). Pennec (2006) proposed a generalisation of the normal distribution based on the maximisation of the entropy knowing the mean and covariance, often referred as *Riemannian normal*. Such a distribution is used in the Poincaré half-plane as a hyper-prior distribution on a mean and standard deviation parameters of a univariate normal (Said et al., 2014). The author derived the normalising constant (for dimension 2) and proposed an algorithm for computing maximum likelihood estimates. It is also mentioned in Ovinnikov (2018) on the Poincaré ball, yet their proposed sampling scheme yield a different distribution due to the linear reparametrisation of the dispersion. Hauberg (2018) derived an efficient sampling scheme and the normalising constant for the *Riemannian normal* defined on the hypersphere. Another major class of manifold distributions are *wrapped* distributions, i.e. push-forward of distributions defined on a tangent space. The *wrapped* normal is a particular case where a normal distribution is considered in the tangent space. Such a class of distribution has been used in an auto-encoder framework on the *hyperboloid* model (of hyperbolic geometry) (Grattarola et al., 2018; Nagano et al., 2019) and on Lie groups (Falorsi et al., 2018).

## 5 EXPERIMENTS

We implemented our model and ran our experiments within the automatic differentiation framework PyTorch (Paszke et al., 2017). We will release the code imminently. Experimental details are fully described in Appendix C.

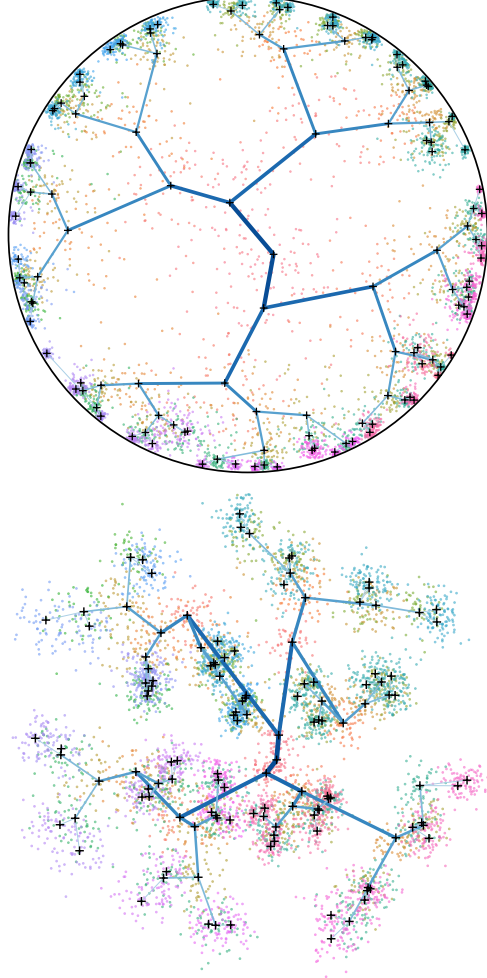


Figure 5: Latent representations of a  $-\mathcal{P}^1$ -VAE (Top) and a  $\mathcal{N}$ -VAE (Bottom), trained on the synthetic dataset. Posterior means are represented by black crosses, and colour dots are posterior samples. Blue lines represent the true underlying hierarchy.

### 5.1 BRANCHING DIFFUSION PROCESS

To test our  $\mathcal{P}^c$ -VAE model on data with underlying hierarchical structure, we generate a synthetic dataset from a branching diffusion process. Nodes  $\mathbf{y}_i \in \mathbb{R}^n$  are normally distributed with mean given by their parent and with unit variance. At every node, 5 observations  $(\mathbf{x}_{i,1}, \dots, \mathbf{x}_{i,5})$  are sampled from a normal distribution with mean given by the node  $\mathbf{y}_i$  and variance  $1/5$ . Models are trained on the vector representations  $(\mathbf{x}_1, \dots, \mathbf{x}_N)$ , hence do not have access to the true hierarchical representation. We restrict ourselves to the Poincaré disc  $\mathbb{B}_c^2$ , and to the *Riemannian* normal as prior and variational posterior distributions. We train several  $\mathcal{P}^c$ -VAEs with increasing curvatures, along with a vanilla  $\mathcal{N}$ -VAE as a baseline.

Table 1: Negative test marginal likelihood estimates on the synthetic dataset. Confidence intervals are computed over 20 runs. The smaller the better. Twenty different datasets are thus generated and models are trained on those.

		Models					
		$\mathcal{N}$ -VAE	$\mathcal{P}^{0.1}$ -VAE	$\mathcal{P}^{0.3}$ -VAE	$\mathcal{P}^{0.8}$ -VAE	$\mathcal{P}^{1.0}$ -VAE	$\mathcal{P}^{1.2}$ -VAE
$\mathcal{L}_{\text{IWAE}}$	$\sigma$	$57.14 \pm .20$	$57.10 \pm .18$	$57.16 \pm .18$	$56.88 \pm .20$	$56.71 \pm .19$	$56.58 \pm .22$
$\mathcal{L}_{\text{IWAE}}$	1.3	$57.03 \pm .20$	$56.91 \pm .18$	$56.91 \pm .18$	$56.39 \pm .19$	$56.21 \pm .20$	$56.07 \pm .22$
$\mathcal{L}_{\text{IWAE}}$	1.7	$57.00 \pm .18$	$56.77 \pm .18$	$56.62 \pm .16$	$55.90 \pm .22$	$55.70 \pm .19$	<b><math>55.60 \pm .18</math></b>

Table 1 shows that the  $\mathcal{P}^c$ -VAE outperforms its Euclidean counterpart in terms of test marginal likelihood. As expected, we observe that as the curvature  $c$  decreases, the performance of the  $\mathcal{N}$ -VAE is recovered. Also, we noticed that increasing the prior distribution distortion  $\sigma_0$  helped embeddings to lie closer to the border, and as a consequence improved generalisation performance. Figure 5 shows that a hierarchical structure is learned by both models, yet  $\mathcal{P}^c$ -VAE’s latent representation may be qualitatively more pleasing. Extra qualitative plots can be found in Figures 7, 8 and 9 in Appendix.

## 5.2 MNIST

The MNIST dataset (LeCun and Cortes, 2010) contains 60,000 training and 10,000 test images of ten handwritten digits (zero to nine), with 28x28 pixels. We empirically test whether a notion of hierarchy exists in those handwritten digits and whether our model can take advantage of such potential structure. We also assess potential differences in performance between  $\mathcal{P}$ -VAEs using *Riemannian* and *wrapped* hyperbolic normal distributions.

Table 3 shows that our model outperforms its Euclidean counterpart, especially for low latent dimensions. This can be interpreted through an information bottleneck perspective; as the latent dimensionality increases, the pressure on the embeddings quality decreases, hence the gain from the hyperbolic geometry is reduced. Such a result is in line with empirical observations from Nickel and Kiela (2017). Also, it appears that the *Riemannian normal* distribution achieves slightly better results than the *wrapped normal* on that dataset. Yet, our current implementation of the *Riemannian normal* gets unstable as the curvature and the dimensionality increase.

We explore the learned latent representations of the trained  $\mathcal{P}$ -VAE and  $\mathcal{N}$ -VAE models in Figure 6. Our  $\mathcal{P}$ -VAE produces a clearer partitioning of the digits, in groupings of  $\{4, 7, 9\}$ ,  $\{0, 6\}$ ,  $\{2, 3, 5, 8\}$  and  $\{1\}$ , with right-slanting  $\{5, 8\}$  being placed separately from the non-slanting ones. Recall that distances become further towards the edge of the Poincaré ball. Similar groupings

appear in the  $\mathcal{N}$ -VAE representation, though the clusterings are perhaps qualitatively more mixed. We quantitatively assess the quality of the learned representations by training a classifier which maps embeddings to digit labels. Table 2 shows that the embeddings learned by our  $\mathcal{P}$ -VAE model yield on average an 2% increase in accuracy over the digits. The full confusion matrices are shown in Figure 10 in Appendix.

Table 2: Per digit accuracy, in percentages, of a classifier trained on the VAEs learned latent embeddings. 20 sets of embeddings are learned by training 10  $\mathcal{N}$ -VAE and 10  $\mathcal{P}^{1.4}$ -VAE models with latent dimension  $d = 2$ . Results are averaged over the 10 sets of embeddings and over 5 trainings of the classifier. The higher the better.

Digits	0	1	2	3	4	5	6	7	8	9	Avg
$\mathcal{N}$ -VAE	89	97	81	75	59	43	89	<b>78</b>	68	<b>57</b>	73.6
$\mathcal{P}^{1.4}$ -VAE	<b>94</b>	97	<b>82</b>	<b>79</b>	<b>69</b>	<b>47</b>	<b>90</b>	77	68	53	<b>75.6</b>

## 6 DISCUSSION

In this paper we have explored VAEs with a Poincaré ball latent space. We derived the necessary ingredients for training such VAEs, namely efficient and reparametrisable sampling schemes, along with probability density functions, for the maximum-entropy and wrapped isotropic normal distributions defined on the Poincaré ball. We empirically demonstrated that endowing a VAE with a Poincaré ball latent space can be beneficial in terms of model generalisation and can yield more interpretable representations if the data has hierarchical structure.

There are a number of interesting future directions. It would be interesting to consider principled ways of assessing whether a given dataset has an underlying hierarchical structure. In the same way that topological data analysis (Pascucci et al., 2011) try to discover the topologies that underlie datasets, it would be interesting to consider methods to discover the underlying geometries. Finally, it would be interesting to extend our derivations for sam-

Table 3: Negative test marginal likelihood estimates computed with 5000 samples. Confidence intervals are computed over 10 runs. \* indicates settings numerically too unstable to obtain sensible results.

		Dimensionality				
		c	2	5	10	20
<b><math>\mathcal{N}</math>-VAE</b>	(0)	144.51 $\pm$ .37	114.66 $\pm$ .08	100.16 $\pm$ .08	97.64 $\pm$ .04	
	0.1	143.87 $\pm$ .47	115.49 $\pm$ .27	100.22 $\pm$ .06	97.22 $\pm$ .05	
<b><math>\mathcal{P}</math>-VAE (Wrapped)</b>	0.2	144.22 $\pm$ .54	115.29 $\pm$ .28	100.06 $\pm$ .13	97.15 $\pm$ .04	
	0.7	143.82 $\pm$ .56	115.08 $\pm$ .31	100.19 $\pm$ .11	97.49 $\pm$ .04	
	1.4	143.97 $\pm$ .61	114.73 $\pm$ .16	100.69 $\pm$ .13	97.99 $\pm$ .06	
	0.1	143.67 $\pm$ .59	115.18 $\pm$ .20	99.90 $\pm$ .14	<b>96.97 <math>\pm</math> .05</b>	
<b><math>\mathcal{P}</math>-VAE (Riemannian)</b>	0.2	143.77 $\pm$ .42	114.69 $\pm$ .25	<b>99.68 <math>\pm</math> .15</b>	97.43 $\pm$ .12	
	0.7	143.05 $\pm$ .41	<b>114.13 <math>\pm</math> .21</b>	101.16 $\pm$ .18	*	
	1.4	<b>142.46 <math>\pm</math> .40</b>	115.48 $\pm$ .32	*	*	

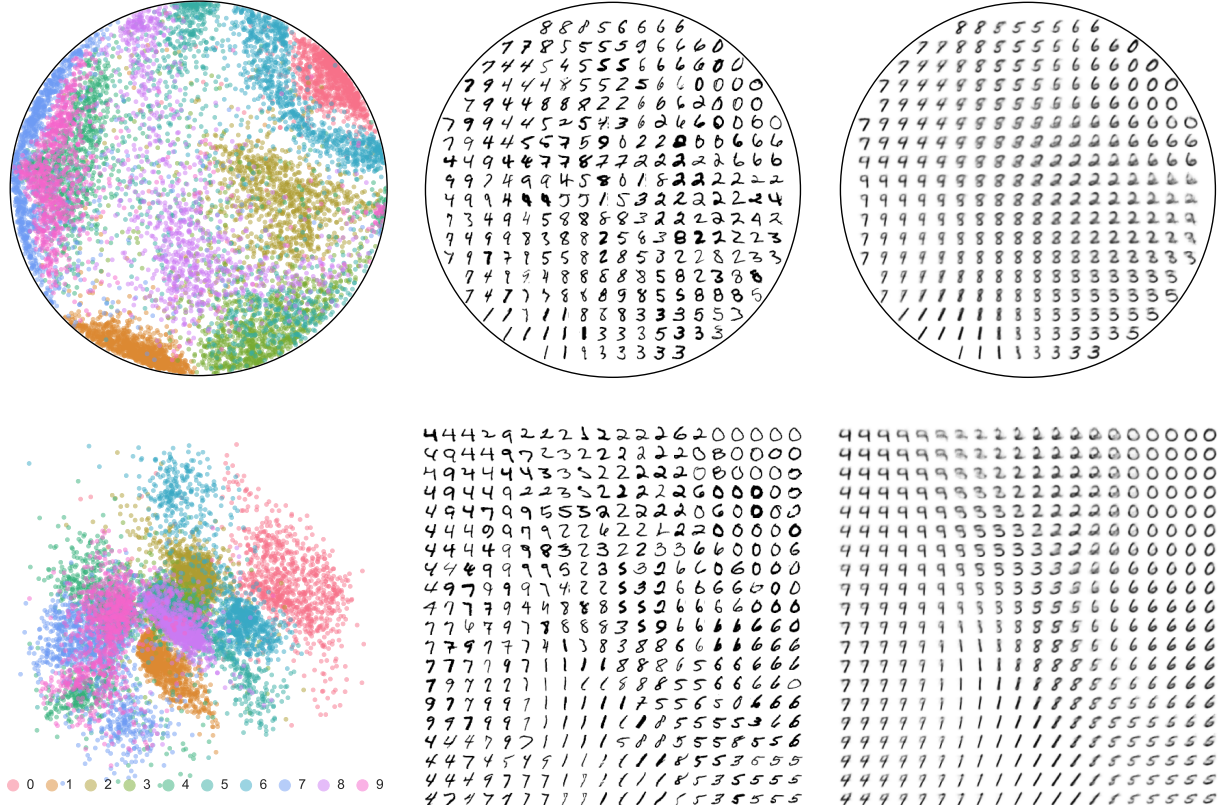


Figure 6: Posterior mean (Left) Sub-sample of digit images associated with posteriors mean (Middle) Model samples (Right) – for  $\mathcal{P}^{1.4}$ -VAE (Top) and  $\mathcal{N}$ -VAE (Bottom).

pling schemes and probability density functions for the Riemannian normal distribution to non-isotropic cases, and to explore implementations that are more numerically stable in higher dimensions.

## Acknowledgments

We are extremely grateful to Adam Foster, Phillippe Gagnon and Emmanuel Chevallier for their help. EM, YWT’s research leading to these results received funding from the European Research Council under the European Union’s Seventh Framework Programme (FP7/2007–2013) ERC grant agreement no. 617071 and they acknowledge Microsoft Research and EPSRC for funding EM’s studentship, and EPSRC grant agreement no. EP/N509711/1 for funding CL’s studentship.

## REFERENCES

Beltrami, E. (1868). *Teoria fondamentale degli spazii di curvatura costante: memoria*. F. Zanetti.

Bengio, Y., Courville, A., and Vincent, P. (2013). Representation learning: A review and new perspectives. *IEEE Trans. Pattern Anal. Mach. Intell.*, 35(8):1798–1828.

Box, G. E. P. and Muller, M. E. (1958). A note on the generation of random normal deviates. *Ann. Math. Statist.*, 29(2):610–611.

Chamberlain, B. P., Clough, J., and Deisenroth, M. P. (2017). Neural Embeddings of Graphs in Hyperbolic Space. *arXiv.org*.

Chevallier, E., Barbaresco, F., and Angulo, J. (2015). Probability density estimation on the hyperbolic space applied to radar processing. In Nielsen, F. and Barbaresco, F., editors, *Geometric Science of Information*, pages 753–761, Cham. Springer International Publishing.

Coates, A., Lee, H., and Ng, A. (2011). An analysis of single-layer networks in unsupervised feature learning. In Gordon, G., Dunson, D., and Dudík, M., editors, *Proceedings of the Fourteenth International Conference on Artificial Intelligence and Statistics*, volume 15 of *JMLR Workshop and Conference Proceedings*, pages 215–223. JMLR W&CP.

Collins, A. and Quillian, M. (1969). Retrieval time from semantic memory. *Journal of Verbal Learning and Verbal Behavior*, 8:240–248.

Coxeter, H. S. M. (1942). *Non-Euclidean Geometry*. University of Toronto Press.

Darwin, C. (1859). *On the Origin of Species by Means of Natural Selection*. Murray, London. or the Preservation of Favored Races in the Struggle for Life.

Davidson, T. R., Falorsi, L., De Cao, N., Kipf, T., and Tomczak, J. M. (2018). Hyperspherical Variational Auto-Encoders. *arXiv.org*.

De Sa, C., Gu, A., Re, C., and Sala, F. (2018). Representation Tradeoffs for Hyperbolic Embeddings. *arXiv.org*.

Duda, R. O., Hart, P. E., and Stork, D. G. (2000). *Pattern Classification (2Nd Edition)*. Wiley-Interscience, New York, NY, USA.

Falorsi, L., de Haan, P., Davidson, T. R., De Cao, N., Weiler, M., Forré, P., and Cohen, T. S. (2018). Explorations in Homeomorphic Variational Auto-Encoding. *arXiv e-prints*, page arXiv:1807.04689.

Figurnov, M., Mohamed, S., and Mnih, A. (2018). Implicit Reparameterization Gradients. *arXiv.org*.

Ganea, O.-E., Bécigneul, G., and Hofmann, T. (2018). Hyperbolic Neural Networks. *arXiv.org*.

Ghahramani, Z., Jordan, M. I., and Adams, R. P. (2010). Tree-structured stick breaking for hierarchical data. In Lafferty, J. D., Williams, C. K. I., Shawe-Taylor, J., Zemel, R. S., and Culotta, A., editors, *Advances in Neural Information Processing Systems 23*, pages 19–27. Curran Associates, Inc.

Grattarola, D., Livi, L., and Alippi, C. (2018). Adversarial Autoencoders with Constant-Curvature Latent Manifolds. *arXiv.org*.

Griffiths, T. L., Jordan, M. I., Tenenbaum, J. B., and Blei, D. M. (2004). Hierarchical topic models and the nested chinese restaurant process. In Thrun, S., Saul, L. K., and Schölkopf, B., editors, *Advances in Neural Information Processing Systems 16*, pages 17–24. MIT Press.

Hauberg, S. (2018). Directional statistics with the spherical normal distribution. In *Proceedings of 2018 21st International Conference on Information Fusion, FUSION 2018*, pages 704–711. IEEE.

Heller, K. A. and Ghahramani, Z. (2005). Bayesian hierarchical clustering. In *Proceedings of the 22Nd International Conference on Machine Learning, ICML '05*, pages 297–304, New York, NY, USA. ACM.

Huang, F. J. and LeCun, Y. (2006). Large-scale learning with SVM and convolutional for generic object categorization. In *CVPR (1)*, pages 284–291. IEEE Computer Society.

Keil, F. (1979). *Semantic and Conceptual Development: An Ontological Perspective*. Cognitive science series. Harvard University Press.

Kingma, D. P. and Ba, J. (2014). Adam: A Method for Stochastic Optimization. *arXiv.org*.

Kingma, D. P. and Welling, M. (2013). Auto-encoding variational bayes. *CoRR*, abs/1312.6114.

Larsen, J., Szymkowiak, A., and Hansen, L. K. (2001). Probabilistic hierarchical clustering with labeled and unlabeled data.

LeCun, Y. and Cortes, C. (2010). MNIST handwritten digit database.

Ley, C. and Verdebout, T. (2017). *Modern Directional Statistics*. New York: Chapman and Hall/CRC.

Linial, N., London, E., and Rabinovich, Y. (1994). The geometry of graphs and some of its algorithmic applications. In *Proceedings of the 35th Annual Symposium on Foundations of Computer Science, SFCS '94*, pages 577–591, Washington, DC, USA. IEEE Computer Society.

Mardia, K. and Jupp, P. (2009). *Directional Statistics*. Wiley Series in Probability and Statistics. Wiley.

Nagano, Y., Yamaguchi, S., Fujita, Y., and Koyama, M. (2019). A Differentiable Gaussian-like Distribution on Hyperbolic Space for Gradient-Based Learning. *arXiv e-prints*, page arXiv:1902.02992.

Nickel, M. and Kiela, D. (2017). Poincaré Embeddings for Learning Hierarchical Representations. *arXiv.org*.

Nickel, M. and Kiela, D. (2018). Learning Continuous Hierarchies in the Lorentz Model of Hyperbolic Geometry. *arXiv.org*.

Ovinnikov, I. (2018). Poincaré Wasserstein Autoencoder. *NeurIPS Workshop on Bayesian Deep Learning*, pages 1–8.

Pascucci, V., Tricoche, X., Hagen, H., and Tierny, J. (2011). *Topological Methods in Data Analysis and Visualization: Theory, Algorithms, and Applications*. Springer Publishing Company, Incorporated, 1st edition.

Paszke, A., Gross, S., Chintala, S., Chanan, G., Yang, E., DeVito, Z., Lin, Z., Desmaison, A., Antiga, L., and Lerer, A. (2017). Automatic differentiation in pytorch. In *NIPS-W*.

Pennec, X. (2006). Intrinsic statistics on riemannian manifolds: Basic tools for geometric measurements. *Journal of Mathematical Imaging and Vision*, 25(1):127.

Petersen, P. (2006). *Riemannian Geometry*. Springer-Verlag New York.

R. Gilks, W. and Wild, P. (1992). Adaptive rejection sampling for gibbs sampling. 41:337–348.

Rezende, D. J., Mohamed, S., and Wierstra, D. (2014). Stochastic Backpropagation and Approximate Inference in Deep Generative Models. *arXiv.org*.

Roy, D. M., Kemp, C., Mansinghka, V. K., and Tenenbaum, J. B. (2006). Learning annotated hierarchies from relational data. In *NIPS*, pages 1185–1192. MIT Press.

Said, S., Bombrun, L., and Berthoumieu, Y. (2014). New riemannian priors on the univariate normal model. *Entropy*, 16(7):4015–4031.

Salakhutdinov, R. R., Tenenbaum, J. B., and Torralba, A. (2011). One-shot learning with a hierarchical nonparametric bayesian model. In *ICML Unsupervised and Transfer Learning*.

Sarkar, R. (2012). Low distortion delaunay embedding of trees in hyperbolic plane. In van Kreveld, M. and Speckmann, B., editors, *Graph Drawing*, pages 355–366, Berlin, Heidelberg. Springer Berlin Heidelberg.

Teh, Y. W., Daume III, H., and Roy, D. M. (2008). Bayesian agglomerative clustering with coalescents. In Platt, J. C., Koller, D., Singer, Y., and Roweis, S. T., editors, *Advances in Neural Information Processing Systems 20*, pages 1473–1480. Curran Associates, Inc.

Tifrea, A., Bécigneul, G., and Ganea, O.-E. (2018). Poincaré GloVe: Hyperbolic Word Embeddings. *arXiv.org*.

Tolstikhin, I., Bousquet, O., Gelly, S., and Schoelkopf, B. (2017). Wasserstein Auto-Encoders. *arXiv.org*.

Ungar, A. A. (2008). A gyrovector space approach to hyperbolic geometry. *Synthesis Lectures on Mathematics and Statistics*, 1(1):1–194.

## A EVIDENCE LOWER BOUND

The ELBO can readily be extended for Riemannian latent spaces by applying Jensen’s inequality w.r.t.  $d\mathcal{M}$  which yield

$$\begin{aligned}
\ln p(\mathbf{x}) &= \ln \int_{\mathbf{z}=\mathcal{M}} p_{\theta}(\mathbf{x}, \mathbf{z}) d\mathcal{M}(\mathbf{z}) \\
&= \ln \int_{\mathcal{M}} p_{\theta}(\mathbf{x}|\mathbf{z}) p(\mathbf{z}) d\mathcal{M}(\mathbf{z}) \\
&= \ln \int_{\mathcal{M}} \frac{p_{\theta}(\mathbf{x}|\mathbf{z}) p(\mathbf{z})}{q_{\phi}(\mathbf{z}|\mathbf{x})} q_{\phi}(\mathbf{z}|\mathbf{x}) d\mathcal{M}(\mathbf{z}) \\
&\geq \int_{\mathcal{M}} \ln \frac{p_{\theta}(\mathbf{x}|\mathbf{z}) p(\mathbf{z})}{q_{\phi}(\mathbf{z}|\mathbf{x})} q_{\phi}(\mathbf{z}|\mathbf{x}) d\mathcal{M}(\mathbf{z}) \\
&= \int_{\mathcal{M}} [\ln p_{\theta}(\mathbf{x}|\mathbf{z}) - \ln p(\mathbf{z}) \\
&\quad - \ln q_{\phi}(\mathbf{z}|\mathbf{x})] q_{\phi}(\mathbf{z}|\mathbf{x}) d\mathcal{M}(\mathbf{z}) \\
&= \mathbb{E}_{\mathbf{z} \sim q_{\phi}(\cdot|\mathbf{x})} [\ln p_{\theta}(\mathbf{x}|\mathbf{z}) + \ln p(\mathbf{z}) - \ln q_{\phi}(\mathbf{z}|\mathbf{x})] \\
&\triangleq \mathcal{L}_{\mathcal{M}}(\mathbf{x}; \theta, \phi)
\end{aligned}$$

## B HYPERBOLIC NORMAL DISTRIBUTIONS

### B.1 PROBABILITY MEASURES ON RIEMANNIAN MANIFOLDS

Probability measures and random vectors can be defined on Riemannian manifolds so as to model uncertainty on non-Euclidean spaces (Pennec, 2006). The Riemannian metric  $G(\mathbf{x})$  induces an infinitesimal volume element on each tangent space  $\mathcal{T}_{\mathbf{x}}\mathcal{M}$ , and thus a measure on the manifold,

$$d\mathcal{M}(\mathbf{x}) = \sqrt{|G(\mathbf{x})|} d\mathbf{x} = \lambda_{\mathbf{x}} d\mathbf{x}, \quad (8)$$

with  $d\mathbf{x}$  being the Lebesgue measure. Random vectors  $\mathbf{x} \in \mathcal{M}$  would naturally be characterised by the Radon-Nikodym derivative of a measure  $\nu$  w.r.t. the Riemannian measure  $d\mathcal{M}(\cdot)$

$$\frac{d\nu(\mathbf{x})}{d\mathcal{M}(\mathbf{x})} = f(\mathbf{x}).$$

Since the normal distribution plays such a canonical role in statistics, generalising it to manifold is of interest. Given a Fréchet expectation  $\mu \in \mathcal{M}$  – defined as minimisers of  $\sigma^2(\mu) = \int_{\mathcal{M}} d\mathcal{M}(\mu, \mathbf{x})^2 p(\mathbf{x}) d\mathcal{M}(\mathbf{x})$  – and a dispersion parameter  $\gamma > 0$  (which is not necessarily

equal to the standard deviation), several properties should be verified by such generalised normal distributions. Such a distribution should tend towards a delta function at  $\mu$  when  $\sigma \rightarrow 0$  and to an (improper for non-compact) uniform distribution when  $\sigma \rightarrow \infty$ . Also, as the curvature tends to 0, one should recover the vanilla normal distribution. Hereby, we review three often used generalisations of the normal distribution, which have different theoretical and computational advantages.

**Maximum entropy normal** The property that Pennec (2006) takes for granted is the maximization of the entropy knowing the mean and the covariance matrix, yielding in the isotropic setting to

$$\begin{aligned} \frac{d\nu^R(\mathbf{x}|\boldsymbol{\mu}, \sigma^2)}{d\mathcal{M}(\mathbf{x})} &= \mathcal{N}_M^R(\mathbf{x}|\boldsymbol{\mu}, \sigma^2) \\ &= \frac{1}{Z^R} \exp\left(-\frac{d_M(\boldsymbol{\mu}, \mathbf{x})^2}{2\sigma^2}\right), \end{aligned} \quad (9)$$

with  $d_M$  being the Riemannian distance on the manifold induced by the tensor metric. The maximum entropy property arises often in physics. Such a formulation – sometimes referred as *Riemannian Normal* distribution – is used by Said et al. (2014) in the Poincaré half-plane, or by Hauberg (2018) in the hypersphere  $\mathbb{S}^d$ . Sampling from such distributions and computing the normalising constant – especially in the anisotropic setting – is usually challenging.

**Wrapped normal** Another generalisation is defined by taking the image by the exponential of a Gaussian distribution on the tangent space centered at the mean value. Such a distribution has been referred as *wrapped*, *push-forward*, *exp-map* or *tangential* normal distribution. Sampling is straightforward, since to obtain a sample  $\mathbf{x}$  one can perform the following scheme

$$\mathbf{x} = \exp_{\boldsymbol{\mu}}^c\left(\frac{\boldsymbol{\epsilon}}{\lambda_{\boldsymbol{\mu}}^c}\right) \quad \text{with } \boldsymbol{\epsilon} \sim \mathcal{N}(\cdot | \mathbf{0}, \sigma^2). \quad (10)$$

The pdf is then readily available through the change of variable formula if one can compute the Jacobian of the exponential map (or its inverse). Hence such a distribution is attractive from a computational perspective. Grattarola et al. (2018) and Nagano et al. (2019) rely on such a distribution defined on the hyperboloid model. Wrapped distributions (not necessarily normal) are often encountered in the *directional* statistics (Ley and Verdebout, 2017; Hauberg, 2018).

**Restricted normal** What is more, for manifold embedded in a vector space, one can consider the restriction of

a normal distribution pdf to the manifold. This yield the Von Mises distribution on  $\mathbb{S}^1$  and the Von Mises-Fisher distribution on  $\mathbb{S}^d$  and on the Stiefel manifold (Hauberg, 2018). Such distributions hence consider a *flat* metric instead of the true manifold metric.

## B.2 MAXIMUM ENTROPY HYPERBOLIC NORMAL DISTRIBUTIONS

In the Poincaré ball  $\mathbb{B}_c^d$ , the maximum entropy generalisation of the normal distribution from Eq 9 yield

$$\begin{aligned} \frac{d\nu^R(\mathbf{x}|\boldsymbol{\mu}, \sigma^2)}{d\mathcal{M}(\mathbf{x})} &= \mathcal{N}_{\mathbb{B}_c^d}^R(\mathbf{x}|\boldsymbol{\mu}, \sigma^2) \\ &= \frac{1}{Z^R} \exp\left(-\frac{d_p^c(\boldsymbol{\mu}, \mathbf{x})^2}{2\sigma^2}\right). \end{aligned} \quad (11)$$

Such a pdf can be computed pointwise once  $Z^R$  is known, which we derive in Appendix B.7. A harder task is to efficiently obtain samples from such a distribution. We show in Appendix B.5 that reparametrising that distribution through the exponential map  $\exp_{\boldsymbol{\mu}}^c$  yield an hyperbolic radius  $r = d_p^c(\boldsymbol{\mu}, \mathbf{x})$  with density

$$\rho^R(r) = \frac{\mathbb{1}_{\mathbb{R}_+}(r)}{Z_r} e^{-\frac{r^2}{2\sigma^2}} \left(\frac{\sinh(\sqrt{c}r)}{\sqrt{c}}\right)^{d-1} \quad (12)$$

We rely on adaptive rejection sampling (R. Gilks and Wild, 1992) to tackle that density as described in Appendix B.8.

## B.3 WRAPPED HYPERBOLIC NORMAL DISTRIBUTIONS

The *wrapped normal* distribution considers a normal distribution in the tangent space  $\mathcal{T}_{\boldsymbol{\mu}}\mathbb{B}_c^d$ . Hence the hyperbolic radius  $r = d_p^c(\boldsymbol{\mu}, \mathbf{x})$  density is given by

$$\rho^W(r) = \frac{\mathbb{1}_{\mathbb{R}_+}(r)}{Z_r} e^{-\frac{r^2}{2\sigma^2}} r^{d-1} \quad (13)$$

As a consequence, the pdf of that distribution is given by

$$\begin{aligned} \frac{d\nu^W(\mathbf{x}|\boldsymbol{\mu}, \sigma^2)}{d\mathcal{M}(\mathbf{x})} &= \mathcal{N}_{\mathbb{B}_c^d}^W(\mathbf{x}|\boldsymbol{\mu}, \sigma^2) \\ &= \mathcal{N}_{\mathbb{B}_c^d}^R(\mathbf{x}|\boldsymbol{\mu}, \sigma^2) \\ &\times \left(d_p^c(\boldsymbol{\mu}, \mathbf{x})\right)^{d-1} \left(\frac{\sinh(\sqrt{c} d_p^c(\boldsymbol{\mu}, \mathbf{x}))}{\sqrt{c}}\right)^{-(d-1)} \\ &= \frac{1}{Z^W} \exp\left(-\frac{d_p^c(\boldsymbol{\mu}, \mathbf{x})^2}{2\sigma^2}\right) \\ &\times \left(d_p^c(\boldsymbol{\mu}, \mathbf{x}) \frac{\sqrt{c}}{\sinh(\sqrt{c} d_p^c(\boldsymbol{\mu}, \mathbf{x}))}\right)^{d-1}. \end{aligned} \quad (14)$$

with  $Z^W$  the normalising constant of a vanilla multivariate normal distribution.

Indeed, plugging this pdf in the expression derived in Appendix yield the expected result. As  $c$  and  $\sigma$  get smaller (resp. bigger), the *wrapped normal* pdf gets closer (resp. further) to the *Riemannian* normal pdf.

#### B.4 HYPERBOLIC POLAR COORDINATES

Euclidean polar coordinates (or hyperspherical coordinate in  $d > 2$ ), express points  $\mathbf{x} \in \mathbb{R}^d$  through a radius  $r \geq 0$  and a direction  $\boldsymbol{\alpha} \in \mathbb{S}^{d-1}$  such that  $\mathbf{x} = r\boldsymbol{\alpha}$ . Yet, one could choose another *pole* (or *reference point*)  $\boldsymbol{\mu} \neq \mathbf{0}$  such that  $\mathbf{x} = \boldsymbol{\mu} + r\boldsymbol{\alpha}$ . Consequently,  $r = d_E(\boldsymbol{\mu}, \mathbf{x})$ . An analogous change of variables can also be constructed in Riemannian manifolds relying on the exponential map as a generalisation of the addition operator. Given a *pole*  $\boldsymbol{\mu} \in \mathbb{B}_c^d$ , the point of hyperbolic polar coordinates  $\mathbf{x} = (r, \boldsymbol{\alpha})$  is defined as the point at distance  $r \geq 0$  of  $\boldsymbol{\mu}$  and lying on the geodesic with initial direction  $\boldsymbol{\alpha} \in \mathbb{S}^{d-1}$ . Hence  $\mathbf{x} = \exp_{\boldsymbol{\mu}}^c(\frac{r}{\lambda_{\boldsymbol{\mu}}^c} \boldsymbol{\alpha})$  with  $\frac{r}{\lambda_{\boldsymbol{\mu}}^c} \boldsymbol{\alpha} \in \mathcal{T}_{\boldsymbol{\mu}} \mathbb{B}_c^d$ , since  $d_p^c(\boldsymbol{\mu}, \mathbf{x}) = \|\ln_{\boldsymbol{\mu}}^c(\mathbf{x})\|_{\boldsymbol{\mu}} = \|\frac{r}{\lambda_{\boldsymbol{\mu}}^c} \boldsymbol{\alpha}\|_{\boldsymbol{\mu}} = r$ .

Below we derive the expression of the Poincaré ball metric in such hyperbolic polar coordinate, for the specific setting where  $\boldsymbol{\mu} = \mathbf{0}$ :  $\mathbf{x} = \exp_{\mathbf{0}}^c(\frac{r}{2} \boldsymbol{\alpha})$ . Switching to Euclidean polar coordinate yield

$$\begin{aligned} ds_{\mathbb{B}_c^d}^2 &= (\lambda_{\mathbf{x}}^c)^2 (dx_1^2 + \cdots + dx_d^2) \\ &= \frac{4}{(1 - c\|\mathbf{x}\|^2)^2} d\mathbf{x}^2 \\ &= \frac{4}{(1 - c\rho^2)^2} (d\rho^2 + \rho^2 ds_{\mathbb{S}^{d-1}}^2). \end{aligned} \quad (15)$$

Let's define  $r = d_p^c(\mathbf{0}, \mathbf{x}) = L(\gamma)$ , with  $\gamma$  being the geodesic joining  $\mathbf{0}$  and  $\mathbf{x}$ . Since such a geodesic is the segment  $[\mathbf{0}, \mathbf{x}]$ , we have

$$\begin{aligned} r &= \int_0^{\rho} \lambda_t^c dt = \int_0^{\rho} \frac{2}{1 - ct^2} dt = \int_0^{\sqrt{c}\rho} \frac{2}{1 - t^2} \frac{dt}{\sqrt{c}} \\ &= \frac{2}{\sqrt{c}} \tanh^{-1}(\sqrt{c}\rho). \end{aligned}$$

Plugging  $\rho = \frac{1}{\sqrt{c}} \tanh(\sqrt{c}\frac{r}{2})$  (and  $d\rho = (1 - c\rho^2)/2dr$ )

into Eq 15 yield

$$\begin{aligned} ds_{\mathbb{B}_c^d}^2 &= \frac{4}{(1 - c\rho^2)^2} \frac{1}{4} (1 - c\rho^2)^2 dr^2 \\ &\quad + \left( 2 \frac{\rho}{1 - c\rho^2} \right)^2 ds_{\mathbb{S}^{d-1}}^2 \\ &= dr^2 + \left( 2 \frac{\frac{1}{\sqrt{c}} \tanh(\sqrt{c}\frac{r}{2})}{1 - c \left( \frac{1}{\sqrt{c}} \tanh(\sqrt{c}\frac{r}{2}) \right)^2} \right)^2 ds_{\mathbb{S}^{d-1}}^2 \\ &= dr^2 + \left( \frac{1}{\sqrt{c}} \sinh(\sqrt{c}r) \right)^2 ds_{\mathbb{S}^{d-1}}^2. \end{aligned} \quad (16)$$

Below we remind the result for the general setting where  $\boldsymbol{\mu} \neq \mathbf{0}$ . In an orthonormal basis of  $\mathcal{T}_{\boldsymbol{\mu}} \mathbb{B}_c^d$  – given by hyperspherical coordinate  $\mathbf{v} = r\boldsymbol{\alpha}$  with  $r \geq 0$  and  $\boldsymbol{\alpha} \in \mathbb{S}^{d-1}$  – the hyperbolic polar coordinate leads to the following expression of the matrix of the metric (Chevallier et al., 2015)

$$G(\mathbf{v}) = G(r) = \begin{pmatrix} 1 & 0 \\ 0 & \left( \frac{\sinh(\sqrt{c}r)}{\sqrt{c}r} \right)^2 \mathbf{I}_{d-1} \end{pmatrix} \quad (17)$$

Hence

$$\sqrt{|G(\mathbf{v})|} = \sqrt{|G(r)|} = \left( \frac{\sinh(\sqrt{c}r)}{\sqrt{c}r} \right)^{d-1}. \quad (18)$$

The fact that the length element  $ds_{\mathbb{B}_c^d}^2$  and equivalently the metric  $G$  only depends on the radius on hyperbolic polar coordinate, is a consequence of the hyperbolic space's isotropy.

#### B.5 PROBABILITY DENSITY FUNCTION

By integrating the density  $f(\mathbf{x}) = \mathcal{N}_{\mathcal{M}}^R(\mathbf{x}|\boldsymbol{\mu}, \sigma^2)$  in the tangent space  $\mathcal{T}_{\boldsymbol{\mu}} \mathbb{B}_c^d$  we get

$$\begin{aligned} &\int_{\mathbb{B}_c^d} f(\mathbf{x}) d\mathcal{M}(\mathbf{x}) \\ &= \int_{\mathbb{B}_c^d} f(\mathbf{x}) \sqrt{|G(\mathbf{x})|} d\mathbf{x} \\ &= \int_{\mathcal{T}_{\boldsymbol{\mu}} \mathbb{B}_c^d} f(\mathbf{v}) \sqrt{|G(\mathbf{v})|} d\mathbf{v} \\ &= \int_{\mathbb{R}_+} \int_{\mathbb{S}^{d-1}} f(r) \sqrt{|G(r)|} dr r^{d-1} ds_{\mathbb{S}^{d-1}} \\ &= \int_{\mathbb{R}_+} \int_{\mathbb{S}^{d-1}} f(r) \left( \frac{\sinh(\sqrt{c}r)}{\sqrt{c}r} \right)^{d-1} dr r^{d-1} ds_{\mathbb{S}^{d-1}} \\ &= \int_{\mathbb{R}_+} \int_{\mathbb{S}^{d-1}} f(r) \left( \frac{\sinh(\sqrt{c}r)}{\sqrt{c}} \right)^{d-1} dr ds_{\mathbb{S}^{d-1}}. \end{aligned}$$

plugging the hyperbolic normal density  $f$ , with the hyperbolic distance  $r = d_p^c(\boldsymbol{\mu}, \mathbf{x})$ , yields

$$\begin{aligned} &= \int_{\mathbb{R}_+} \int_{\mathbb{S}^{d-1}} \frac{1}{Z^R} e^{-\frac{r^2}{2\sigma^2}} \left( \frac{\sinh(\sqrt{c}r)}{\sqrt{c}} \right)^{d-1} dr ds_{\mathbb{S}^{d-1}} \\ &= \frac{1}{Z^R} \left( \int_{\mathbb{R}_+} e^{-\frac{r^2}{2\sigma^2}} \left( \frac{\sinh(\sqrt{c}r)}{\sqrt{c}} \right)^{d-1} dr \right) A_{\mathbb{S}^{d-1}} \\ &= \frac{1}{Z^R} Z_r^R A_{\mathbb{S}^{d-1}} \\ \Leftrightarrow & Z^R = Z_r^R A_{\mathbb{S}^{d-1}}. \end{aligned}$$

Hence, with the hyperbolic polar change of coordinates,  $\mathcal{N}_{\mathcal{M}}^R(\mathbf{x}|\boldsymbol{\mu}, \sigma^2) \sqrt{|G(\mathbf{x})|}$  factorises as  $\rho^R(r) \times 1_{\mathbb{S}^{d-1}}(\boldsymbol{\alpha})$  with  $\boldsymbol{\alpha}$  being uniformly distributed on the hypersphere  $\mathbb{S}^{d-1}$ , and the hyperbolic radius  $r = d_p^c(\boldsymbol{\mu}, \mathbf{x})$  being distributed according to the density (w.r.t the Lebesgue measure)

$$\rho^R(r) = \frac{\mathbb{1}_{\mathbb{R}_+}(r)}{Z_r^R} e^{-\frac{r^2}{2\sigma^2}} \left( \frac{\sinh(\sqrt{c}r)}{\sqrt{c}} \right)^{d-1} \quad (19)$$

The vanilla Gaussian density is recovered as  $c \rightarrow 0$  since  $\left( \frac{\sinh(\sqrt{c}r)}{\sqrt{c}} \right)^{d-1} \rightarrow r^{d-1}$ .

By expanding the sinh term using the binomial formula, we get

$$\begin{aligned} \rho^R(r) &= \frac{\mathbb{1}_{\mathbb{R}_+}(r)}{Z_r^R} e^{-\frac{r^2}{2\sigma^2}} \left( \frac{\sinh(\sqrt{c}r)}{\sqrt{c}} \right)^{d-1} \\ &= \frac{\mathbb{1}_{\mathbb{R}_+}(r)}{Z_r^R} e^{-\frac{r^2}{2\sigma^2}} \left( \frac{e^{\sqrt{c}r} - e^{-\sqrt{c}r}}{2\sqrt{c}} \right)^{d-1} \\ &= \frac{\mathbb{1}_{\mathbb{R}_+}(r)}{Z_r^R} e^{-\frac{r^2}{2\sigma^2}} \frac{1}{(2\sqrt{c})^{d-1}} \\ &\quad \times \sum_{k=0}^{d-1} \binom{d-1}{k} (e^{\sqrt{c}r})^{d-1-k} (-e^{-\sqrt{c}r})^k \\ &= \frac{\mathbb{1}_{\mathbb{R}_+}(r)}{Z_r^R} \frac{1}{(2\sqrt{c})^{d-1}} e^{-\frac{r^2}{2\sigma^2}} \\ &\quad \times \sum_{k=0}^{d-1} (-1)^k \binom{d-1}{k} e^{(d-1-2k)\sqrt{c}r} \\ &= \frac{\mathbb{1}_{\mathbb{R}_+}(r)}{Z_r^R} \frac{1}{(2\sqrt{c})^{d-1}} \\ &\quad \times \sum_{k=0}^{d-1} (-1)^k \binom{d-1}{k} e^{-\frac{r^2}{2\sigma^2} + (d-1-2k)\sqrt{c}r} \\ &= \frac{\mathbb{1}_{\mathbb{R}_+}(r)}{Z_r^R} \frac{1}{(2\sqrt{c})^{d-1}} \sum_{k=0}^{d-1} (-1)^k \binom{d-1}{k} \\ &\quad \times e^{\frac{(d-1-2k)^2}{2} c\sigma^2} e^{-\frac{1}{2\sigma^2} [r - (d-1-2k)\sqrt{c}\sigma^2]^2}. \end{aligned} \quad (20)$$

## B.6 CUMULATIVE DENSITY FUNCTION

Integrating the expended density of Eq (20) yields

$$\begin{aligned} F_r^R(r) &= \int_{-\infty}^r \rho^R(r) dr \\ &= \frac{1}{Z_r^R} \frac{1}{(2\sqrt{c})^{d-1}} \sum_{k=0}^{d-1} (-1)^k \binom{d-1}{k} e^{\frac{(d-1-2k)^2}{2} c\sigma^2} \\ &\quad \times \int_0^r e^{-\frac{1}{2\sigma^2} [r - (d-1-2k)\sqrt{c}\sigma^2]^2} dr \\ &\quad \times \sum_{k=0}^{d-1} (-1)^k \binom{d-1}{k} e^{\frac{(d-1-2k)^2}{2} c\sigma^2} \\ &\quad \times \left[ \operatorname{erf} \left( \frac{r - (d-1-2k)\sqrt{c}\sigma^2}{\sqrt{2}\sigma} \right) \right. \\ &\quad \left. + \operatorname{erf} \left( \frac{(d-1-2k)\sqrt{c}\sigma^2}{\sqrt{2}} \right) \right] \end{aligned} \quad (21)$$

with  $\Phi : x \mapsto \frac{1}{2} \left( 1 + \operatorname{erf} \left( \frac{x}{\sqrt{2}} \right) \right)$ , the cumulative distribution function of a standard normal distribution.

## B.7 NORMALISATION CONSTANT

As shown in Appendix B.4 – by using hyperbolic polar coordinate – the density of the hyperbolic normal distribution factorises between a hyperbolic radius  $r$  and a direction  $\boldsymbol{\alpha}$ , thus

$$Z^R = Z_r^R Z_{\boldsymbol{\alpha}} \quad (22)$$

We know that the surface area of the  $d-1$ -dimensional hypersphere with radius 1 is given by

$$Z_{\boldsymbol{\alpha}} = A_{\mathbb{S}^{d-1}} = \frac{2\pi^{d/2}}{\Gamma(d/2)}. \quad (23)$$

Also, taking the limit  $F_r^R(r) \xrightarrow[r \rightarrow \infty]{} 1$  in Eq (21) yield

$$\begin{aligned} Z_r^R &= \sqrt{\frac{\pi}{2}} \sigma \frac{1}{(2\sqrt{c})^{d-1}} \sum_{k=0}^{d-1} (-1)^k \binom{d-1}{k} \\ &\quad \times e^{\frac{(d-1-2k)^2}{2} c\sigma^2} \left[ 1 + \operatorname{erf} \left( \frac{(d-1-2k)\sqrt{c}\sigma^2}{\sqrt{2}} \right) \right]. \end{aligned} \quad (24)$$

Note that by the antisymmetry of  $\operatorname{erf}$ , one can simplify Eq 24 with a sum over  $\lceil d/2 \rceil$  terms. Also, computing such a sum is much more stable by relying on the *log sum exp* trick.

For the special case of  $c = 1$  and  $d = 2$  we recover the formula given in Said et al. (2014)

$$Z_r^R = \sqrt{\frac{\pi}{2}} \sigma e^{\frac{\sigma^2}{2}} \operatorname{erf} \left( \frac{\sigma}{\sqrt{2}} \right). \quad (25)$$

## B.8 SAMPLING

In this section we detail the sampling scheme that we use for the Riemannian normal distribution  $\mathcal{N}_{\mathbb{B}_c^d}^R(\cdot|\boldsymbol{\mu}, \sigma^2)$ , along with a reparametrisation allowing to compute gradients with respect to the parameters  $\boldsymbol{\mu}$  and  $\sigma$ .

**Reparametrisation** Analogously to the Box-Muller transform (Box and Muller, 1958) for sampling random variables normally distributed, one can make use of hyperbolic polar coordinate to get a factorized density derived in Appendix B.5. We indeed rely on the reparametrisation of  $\mathbf{x} \sim \mathcal{N}_{\mathbb{B}_c^d}^R(\cdot|\boldsymbol{\mu}, \sigma^2)$  given by

$$\mathbf{x} = \exp_{\boldsymbol{\mu}}^c \left( \frac{r}{\lambda_{\boldsymbol{\mu}}^c} \boldsymbol{\alpha} \right),$$

with the direction  $\boldsymbol{\alpha}$  being uniformly distributed on the  $d-1$  hypersphere,

$$\boldsymbol{\alpha} \sim \mathcal{U}(\mathbb{S}^{d-1})$$

and the hyperbolic radius  $r$  having a derivative w.r.t. Lebesgue being

$$\rho^R(r) = \frac{\mathbb{1}_{\mathbb{R}_+}(r)}{Z_r^R} e^{-\frac{r^2}{2\sigma^2}} \left( \frac{\sinh(\sqrt{c}r)}{\sqrt{c}} \right)^{d-1}.$$

Such a density is not a well-known distribution and its cumulative density function does not seem analytically invertible. We therefore rely on a rejection sampling. Yet the difficulty is to find a proposal and derive a tight enough bound such that the acceptance rate behaves well with  $\sigma$ ,  $c$  and  $d$ . We solve that issue by making use of the log concavity of the density as described below.

**Sampling challenges due to the hyperbolic geometry**  
Several properties of the Euclidean space do not generalise to the hyperbolic setting, unfortunately hardening the task of obtaining samples from *Riemannian* normal distributions. First, one can factorise a normal density through the space's dimensions – thanks to the Pythagorean theorem – hence allowing to divide the task on several subspaces and then concatenate the samples. Such a property does not extend to the hyperbolic geometry, thus seemingly preventing us from focusing on 2-dimensional samples. Second, in Euclidean geometry, the polar radius  $r$  is distributed according to  $\rho^W(r) = \frac{\mathbb{1}_{\mathbb{R}_+}(r)}{Z_r^W} e^{-\frac{r^2}{2\sigma^2}} r^{d-1}$ , making it easy by a linear change of variable to take into account different scaling values. The non-linearity of  $\sinh$  prevent us from using such a simple change of variable.

**Computing gradients with respect to parameters** So as to compute gradients of samples  $\mathbf{x}$  with respect to the parameters  $\boldsymbol{\mu}$  and  $\sigma$  of samples of a hyperbolic distributions, we respectively rely on the reparametrisation given by Eq 26 for  $\nabla_{\boldsymbol{\mu}} \mathbf{x}$ , and on an implicit reparametrisation (Figurnov et al., 2018) of  $r$  for  $\nabla_{\sigma} \mathbf{x}$ .

We have  $\mathbf{x} = \exp_{\boldsymbol{\mu}}^c \left( \frac{r}{\lambda_{\boldsymbol{\mu}}^c} \boldsymbol{\alpha} \right)$  with  $\boldsymbol{\alpha} \sim \mathcal{U}(\mathbb{S}^{d-1})$  and  $r \sim \rho^R(\cdot)$ . Hence,

$$\nabla_{\boldsymbol{\mu}} \mathbf{x} = \nabla_{\boldsymbol{\mu}} \exp_{\boldsymbol{\mu}}^c(\boldsymbol{\alpha}), \quad (26)$$

with  $\boldsymbol{v} = \frac{r}{\lambda_{\boldsymbol{\mu}}^c} \boldsymbol{\alpha}$  (actually) independent of  $\boldsymbol{\mu}$ , and

$$\nabla_{\sigma} \mathbf{x} = \nabla_{\sigma} \exp_{\boldsymbol{\mu}}^c(\boldsymbol{v}) = \nabla_{\boldsymbol{v}} \exp_{\boldsymbol{\mu}}^c(\boldsymbol{v}) \frac{\boldsymbol{\alpha}}{\lambda_{\boldsymbol{\mu}}^c} \nabla_{\sigma} r, \quad (27)$$

with  $\nabla_{\sigma}(r)$  computed via the implicit reparametrisation given by

$$\begin{aligned} \nabla_{\sigma}(r) &= -(\nabla_r F^R(r, \sigma))^{-1} \nabla_{\sigma} F^R(r, \sigma) \\ &= -(\rho^R(r; \sigma))^{-1} \nabla_{\sigma} F^R(r, \sigma). \end{aligned} \quad (28)$$

**Adaptive Rejection Sampling** Hence we make use of the log-concavity of  $\rho^R$  by relying a piecewise exponential distribution proposal from adaptive rejection sampling (ARS) (R. Gilks and Wild, 1992). Such a proposal automatically adapt itself with the parameters  $\sigma$ ,  $c$  and  $d$ . Even though  $\mathcal{N}_{\mathbb{B}_c^d}$  is defined on a  $d$ -dimensional manifold,  $\rho^R$  is a univariate distribution hence the sampling scheme is not directly affected by dimensionality.

The difficulty in ARS is to choose the initial set of points to construct the piecewise exponential proposal. To do so, we first compute the mean  $m = \mathbb{E}_{r \sim \rho^R}[r]$  and standard deviation  $s = \mathbb{V}_{r \sim \rho^R}[r]^{1/2}$  of the targeted distribution. Then we choose a grid  $\eta = (\eta_1, \dots, \eta_K) = (\text{linspace}(\eta_{\text{max}}, \eta_{\text{min}}, K/2), \text{linspace}(\eta_{\text{min}}, \eta_{\text{max}}, K/2))$ . Eventually, we set the initial points  $(x_1, \dots, x_K)$  to  $x_k = m + \eta_k * \min(s, 0.95 * m/\eta_{\text{max}})$ . For our experiments we chose  $\eta_{\text{min}} = .1$ ,  $\eta_{\text{max}} = 3$ ,  $K = 20$ .

We do not adapt the proposal within the rejection sampling since we empirically found it unnecessary.

## C EXPERIMENTAL DETAILS

In this section we give more details on the datasets, architecture designs and optimisation schemes used for the experimental results given in Section 5.

## C.1 SYNTHETIC BRANCHING DIFFUSION PROCESS

**Generation** Nodes  $(\mathbf{y}_1, \dots, \mathbf{y}_N) \in \mathbb{R}^n$  of the branching diffusion process are sampled as follow

$$\mathbf{y}_i \sim \mathcal{N}(\cdot | \mathbf{y}_{\pi(i)}, \sigma_0^2) \quad \forall i \in 1, \dots, N$$

with  $\pi(i)$  being the index of the  $i$ th node's ancestor and  $d(i)$  its depth. Then, noisy observations are sampled for each node  $\mathbf{x}_i$ ,

$$\mathbf{x}_{i,j} = \mathbf{y}_i + \epsilon_{i,j}, \quad \epsilon_{i,j} \sim \mathcal{N}(\cdot | \mathbf{0}, \sigma_j^2) \quad \forall i, j.$$

The root  $x_0$  is set to  $\mathbf{0}$  for simplicity. The observation dimension is set to  $n = 50$ . The dataset  $(\mathbf{x}_{i,j})_{i,j}$  is centered and normalised to have unit variance. Thus, the choice of variance  $\sigma_0^2$  does not matter and it is set to  $\sigma_0 = 1$ . The number of noisy observations is set to  $J = 5$ , and its variance to  $\sigma_j^2 = \sigma_0^2/5 = 1/5$ . The depth is set to 6 and the branching factor to 2.

**Architectures** Both  $\mathcal{N}$ -VAE and  $\mathcal{P}^c$ -VAE decoders parametrise the mean of the unit variance Gaussian likelihood  $\mathcal{N}(\cdot | f_\theta(\mathbf{z}), 1)$ . Their encoders parametrise the mean and the log-variance of respectively an isotropic normal distribution  $\mathcal{N}(\cdot | g_\phi(\mathbf{z}))$  and an isotropic hyperbolic normal distribution  $\mathcal{N}_{\mathbb{B}_c^d}(\cdot | g_\phi(\mathbf{z}))$ . The  $\mathcal{N}$ -VAE's encoder and decoder are composed of 2 Fully-Connected layers with a ReLU activation in between, as summed up in Tables 4 and 5. The  $\mathcal{P}^c$ -VAE's design is similar, the differences being that the decoder's output is mapped to manifold via the exponential map  $\exp_0^c$ , and the decoder's first layer is made of *gyroplane units* presented in Section 3.2, as summarised in Tables 6 and 7. Observations live in  $\mathcal{X} = \mathbb{R}^{50}$  and the latent space dimensionality  $d$  is set to  $d = 2$ .

Table 4: Encoder network for  $\mathcal{N}$ -VAE

Layer	Output dim	Activation
Input	50	Identity
FC	200	ReLU
FC	2, 1	Identity

The synthetic datasets are generated as described in Section 5, then centered and normalised to unit variance. There are then randomly split into training and testing datasets with a proportion 0.7.

**Optimisation** Gyroplanes offset  $\mathbf{b} \in \mathbb{B}_c^d$  are only *implicitly* parametrised to live in the manifold, by projecting

Table 5: Decoder network for  $\mathcal{N}$ -VAE

Layer	Output dim	Activation
Input	2	Identity
FC	200	ReLU
FC	50	Identity

Table 6: Encoder network for  $\mathcal{P}^c$ -VAE

Layer	Output dim	Activation
Input	50	Identity
FC	200	ReLU
FC	2, 1	$\exp_0^c$ , Identity

Table 7: Decoder network for  $\mathcal{P}^c$ -VAE

Layer	Output dim	Activation
Input	2	Identity
Gyroplane	200	ReLU
FC	50	Identity

a real vector  $\mathbf{b} = \exp_0^c(\mathbf{b}')$ . Hence, all parameters  $\{\theta, \phi\}$  of the model explicitly live in Euclidean spaces which means that usual optimisation schemes can be applied. We therefore rely on Adam optimiser (Kingma and Ba, 2014) with parameters  $\beta_1 = 0.9$ ,  $\beta_2 = 0.999$  and a constant learning rate set to  $1e-3$ . Models are trained with mini-batches of size 64 for 1000 epochs. The ELBO is approximated with a MC estimate with  $K = 1$ .

## C.2 MNIST DIGITS

**Architectures** The architectures used for the encoder and the decoder for Mnist are similar to the ones used for the Synthetic Branching Diffusion Process. They differ by the dimensions of the observation space ( $\mathcal{X} = \mathbb{R}^{28 \times 28}$ ) and hidden space. The output of the first fully connected layer is here equal to 600. The latent space dimensionality  $d$  is set to 2, 5, 10 and 20 respectively. The bias of the decoder's last layer is set to the average value of digits (for each pixel).

The architectures used for the classifier are similar than the decoder architectures, the only difference being the output dimensionality (10 labels). We initialise the classifier's first layer with decoder's first layer weights. Then the classifier is trained to minimise the cross entropy for 5 epochs, with mini-batches of size 64 and a constant learning rate of  $1e-3$ .

**Optimisation** We set the prior distribution's distortion to  $\sigma = 1$ . We rely on Adam optimiser with parameters  $\beta_1 = 0.9$ ,  $\beta_2 = 0.999$  and a constant learning rate of  $5e^{-4}$ . Models are trained with mini-batches of size 128 for 80 epochs.

## D MORE EXPERIMENTAL QUALITATIVE RESULTS

Figure 7 shows latent representations of  $\mathcal{P}^c$ -VAEs with different curvatures. With "small" curvatures, we observe that embeddings lie close the center of the ball, where the geometry is close to be Euclidean.

Similarly as Figure 7, Figure 8 illustrates the learned latent representations of  $\mathcal{P}^c$ -VAE with decreasing curvatures  $c$ , by highlighting the leaned *gyroplanes* of the decoder.

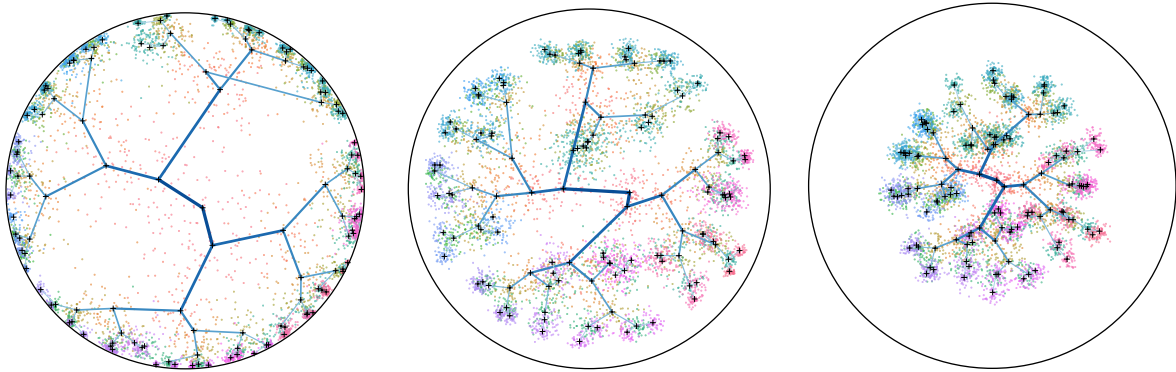


Figure 7: Latent representations of  $\mathcal{P}^c$ -VAE with decreasing curvatures  $c = 1.2, 0.3, 0.1$  (Left to Right).

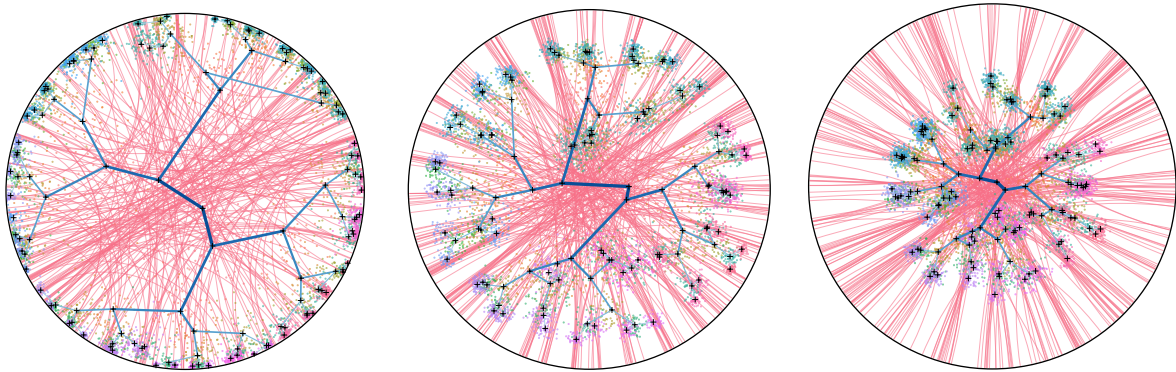


Figure 8: Latent representations of  $\mathcal{P}^c$ -VAE with decreasing curvatures  $c = 1.2, 0.3, 0.1$  (Left to Right).

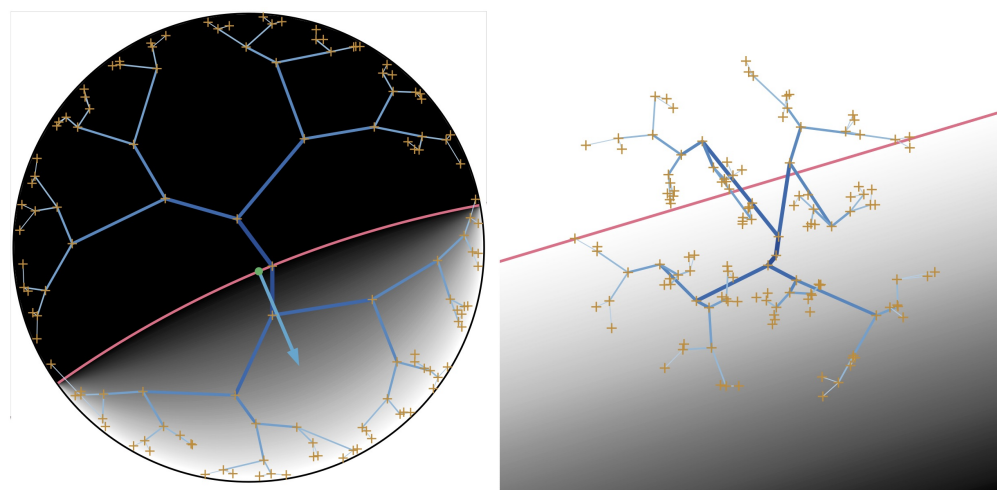


Figure 9: Latent representation of  $\mathcal{P}^1$ -VAE (Left) and  $\mathcal{N}$ -VAE (Right) with heatmap of the log distance to the hyperplane (in pink).

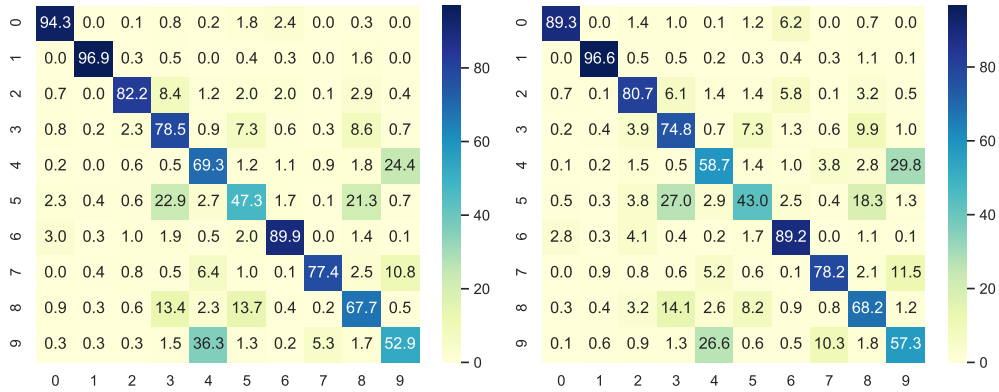


Figure 10: Average confusion matrices of the classifiers trained on embeddings from the  $\mathcal{P}^{1.4}$ -VAE (Left) and  $\mathcal{N}$ -VAE (Right) models.